NAVAL POSTGRADUATE SCHOOL
MONTEREY, CALIFORNIA

THESIS

SYNOPTIC APPLICATIONS OF NOAA MICROWAVE SOUNDING DATA

by

Mark W. Mickelinc

December, 1995

Thesis Co-Advisors: Paul A. Hirschberg
Carlyle H. Wash

Approved for public release; distribution is unlimited.

DISCLAIMER NOTICE

THIS DOCUMENT IS BEST QUALITY AVAILABLE. THE COPY FURNISHED TO DTIC CONTAINED A SIGNIFICANT NUMBER OF PAGES WHICH DO NOT REPRODUCE LEGIBLY.

REPORT DOCUMENTATION PAGE

Form Approved OMB No. 0704-0188

1. AGENCY USE ONLY *(Leave blank)*	2. REPORT DATE	3. REPORT TYPE AND DATES COVERED
	December 1995	Master's Thesis

4. TITLE AND SUBTITLE SYNOPTIC APPLICATIONS OF NOAA MICROWAVE SOUNDING DATA	5. FUNDING NUMBERS
6. AUTHOR Mickelinc, Mark W.	
7. PERFORMING ORGANIZATION NAME(S) AND ADDRESS(ES) Naval Postgraduate School Monterey CA 93943-5000	8. PERFORMING ORGANIZATION REPORT NUMBER
9. SPONSORING/MONITORING AGENCY NAME(S) AND ADDRESS(ES) National Weather Service, Washington, D. C.	10. SPONSORING/MONITORING AGENCY REPORT NUMBER

11. SUPPLEMENTARY NOTES The views expressed in this thesis are those of the author and do not reflect the official policy or position of the Department of Defense or the U.S. Government.

12a. DISTRIBUTION/AVAILABILITY STATEMENT Approved for public release; distribution is unlimited.	12b. DISTRIBUTION CODE

13. ABSTRACT *(maximum 200 words)*

A statistical study of satellite-derived channel 3 Microwave Sounding Unit (MSU) brightness-temperatures and conventionally derived fields by Parke (1994) showed that the MSU can be used to locate baroclinic waves. Most significantly, Parke found high negative average correlations between the synoptic-scale MSU and mid-level height patterns in accordance with theory. However, there were instances in his six-month sample where the correlations were not as expected. In this thesis, three reasons for these unexpected correlations are investigated. One reason is the inclusion of erroneous data. Another is the statistical method. In particular, the Errico (1985) method of scale separation is found to not remove all unwanted wavelength signals in the data. Moreover, the Eulerian-based statistics produce misleading results at times. Results from an example implementation of a simple semi-Lagrangian approach suggests that such a method might produce more reasonable correlations. Thirdly, synoptic regime appears to be a factor. Classifying synoptic regimes with a thermal wind zonal index shows some utility in identifying patterns that are associated with expected correlations. Finally, two case studies are presented that demonstrate the usefulness of MSU data in conjunction with conventional data in individual forecasting situations.

14. SUBJECT TERMS Satellite, Microwave Sounding Unit, Tropopause undulations, Forecasting			15. NUMBER OF PAGES 78 16. PRICE CODE
17. SECURITY CLASSIFICATION OF REPORT Unclassified	18. SECURITY CLASSIFICATION OF THIS PAGE Unclassified	19. SECURITY CLASSIFICATION OF ABSTRACT Unclassified	20. LIMITATION OF ABSTRACT UL

NSN 7540-01-280-5500

Standard Form 298 (Rev. 2-89)
Prescribed by ANSI Std. 239-18 298-102

Approved for public release; distribution is unlimited.

SYNOPTIC APPLICATIONS OF NOAA MICROWAVE SOUNDING DATA

Mark W. Mickelinc
Lieutenant, United States Navy
B.S., University of South Carolina, 1986

Submitted in partial fulfillment
of the requirements for the degree of

MASTER OF SCIENCE IN METEOROLOGY AND PHYSICAL OCEANOGRAPHY

from the

NAVAL POSTGRADUATE SCHOOL
December 1995

Author: 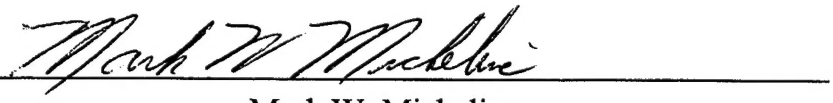
Mark W. Mickelinc

Approved by: 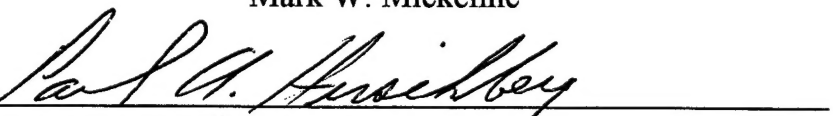
Paul A. Hirschberg, Thesis Co-Advisor

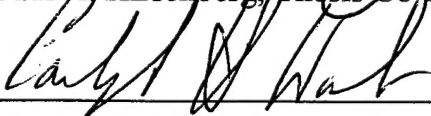
Carlyle H. Wash, Thesis Co-Advisor


Robert L. Haney, Chairman
Department of Meteorology

ABSTRACT

A statistical study of satellite-derived channel 3 Microwave Sounding Unit (MSU) brightness-temperatures and conventionally derived fields by Parke (1994) showed that the MSU can be used to locate baroclinic waves. Most significantly, Parke found high negative average correlations between the synoptic-scale MSU and mid-level height patterns in accordance with theory. However, there were instances in his six-month sample where the correlations were not as expected. In this thesis, three reasons for these unexpected correlations are investigated. One reason is the inclusion of erroneous data. Another is the statistical method. In particular, the Errico (1985) method of scale separation is found to not remove all unwanted wavelength signals in the data. Moreover, the Eulerian-based statistics produce misleading results at times. Results from an example implementation of a simple semi-Lagrangian approach suggests that such a method might produce more reasonable correlations. Thirdly, synoptic regime appears to be a factor. Classifying synoptic regimes with a thermal wind zonal index shows some utility in identifying patterns that are associated with expected correlations. Finally, two case studies are presented that demonstrate the usefulness of MSU data in conjunction with conventional data in individual forecasting situations.

TABLE OF CONTENTS

I. INTRODUCTION

The accurate description of the current state of the atmosphere is paramount to the need of weather forecasters. As numerical weather prediction skill continues to improve with finer resolution, this description becomes increasingly important in establishing the initial conditions. Satellite data has been instrumental in supplementing conventionally retrieved meteorological information. Imagery can show general features, but derived wind and temperature fields from satellites are perhaps more valuable. To a Navy operational forecaster who may have access to satellite information but not to sophisticated numerical model solutions, the ability to link satellite data to conceptual models of meteorological phenomena is likewise important.

A new satellite application is described by Velden (1992). He shows that the 54.96 GHz channel brightness temperature data of the Microwave Sounding Unit (MSU) can be used to locate upper-tropospheric and lower-stratospheric thermal anomalies and consequently, to infer information about the presence of tropopause undulations. These undulations have been shown (Hoskins et al., 1985; Hirschberg and Fritsch, 1991a,b) to be important in the structure and evolution of baroclinic waves and cyclones.

A climatological study that quantitatively extended Velden's investigation of the MSU analysis as a forecasting tool was performed by Parke (1994). He used six months (01 October 1993 to 31 March 1994) of analyses of various conventionally derived fields over a portion of the Northern Hemisphere. These data were statistically correlated with the corresponding analyses of the MSU brightness temperature. High positive spatial and

temporal correlations were obtained between the MSU and the 400-100-mb thickness over all wavelengths in the data. More importantly, relatively high negative MSU-500-mb height correlations for the short (< synoptic scale) wavelengths and high positive MSU-50-mb height correlations for the long (> synoptic scale) wavelengths suggested that upper-level synoptic-scale thermal anomalies are reflected downwards into the middle troposphere. A consequence of this is that it is possible to use MSU data to identify and track mid-level synoptic-scale baroclinic waves. However, there were periods of time in the six-month data set when the synoptic scale MSU-500-mb height correlations were unexpectedly near zero or even positive and the MSU-50-mb height correlations were near zero. During these periods the forecasting utility of the MSU product was poor.

In this thesis, Parke's work is advanced by identifying reasons why his MSU-500-mb and MSU-50-mb height correlations were unexpected at times. In addition, several case studies that clearly demonstrate the use of MSU data in supporting or identifying errors in NWP solutions are presented. The ultimate goal of the thesis is to better understand applications of MSU for weather analysis and forecasting.

II. BACKGROUND

A. DYNAMICS

Quasi-geostrophic (QG) extratropical cyclogenesis models hold that low - level height and pressure changes in developing baroclinic waves are produced by vorticity advection and temperature advection (Holton, 1979). In particular, cold air advection (CAA) in the 1000-500-mb layer behind the surface cyclone causes the thickness of the layer to decrease, which hydrostatically lowers the heights in the layer. However, this argument assumes a fixed lower boundary, usually taken to be 1000 mb, which forces the effects of the CAA to be reflected in the middle troposphere.

Hirschberg and Fritsch (1991a,b) have demonstrated that tropopause-level temperature patterns and advections are important in the hydrostatic structure of extratropical cyclones. Cross sections through developing baroclinic waves often show synoptic-scale undulations along the tropopause. At a steeply inclined tropopause, areas of relatively warm lower stratospheric air are found alongside areas of relatively cool upper tropospheric air. The wind flow during developing situations is usually perpendicular to these contrasting warm and cold pools, which results in large temperature advections. Converse to the traditional (QG) model (Holton, 1979), Hirschberg and Fritsch (1991b) assume and find substantial evidence for a level of insignificant dynamics (LID) at an upper level where heights and pressure patterns are relatively insensitive to the cyclone-scale motions below. Consequently, cyclone-scale warm air advection (WAA) at levels near the tropopause, e.g. 400-100 mb, are

reflected downwards resulting in height and pressure falls at lower levels (Fig. 2.1). More specifically, Hirschberg and Fritsch (1993) show that synoptic-scale temperature anomalies and advection are reflected more downwards than upwards in the height field, while larger-(e. g. planetary) scale anomalies and advection are reflected more upwards. Figure 2.2 is a conceptual diagram of the height features in this upper-tropospheric/lower-stratospheric layer. The upper surface reflects planetary-scale waves while the lower surface reflects both planetary-scale and cyclone-scale waves. This suggests that if we can remove the planetary-scale waves from the lower surface data (e.g. 500 mb) we can track the location and development of cyclone-scale waves at this surface simply by measuring the cyclone-scale layer temperature. Significantly, this process can be monitored by using MSU brightness temperatures (Velden, 1992).

B. REMOTE SENSING

In this thesis, a remote sensing measurement is used to monitor the temperature structure of the atmosphere, based on the atmosphere's radiation characteristics. Molecular oxygen (O_2) is a well-mixed gas in the atmosphere (Machta and Hughes, 1970). By using the absorption and re-emission characteristics of O_2, pressure and temperature as a function of height can be determined for discrete pressure levels (Meeks and Lilley, 1963). In the microwave region, O_2 has an absorption region between 50 and 70 GHz, peaking around 60 GHz. By making observations on the edges of the absorption band, the determination of brightness temperature as a function of height can be made.

Following Spencer et al. (1990), equation (2.1) describes brightness temperature in the oxygen absorption region as,

$$T_b(\nu) = \int_{\ln p_s}^{-\infty} T_p \left[\frac{d\tau_\nu(p)}{d\ln p} \right] d\ln p + \tau_\nu(p_s) T_s \,, \tag{2.1}$$

where T_b is the brightness temperature, ν is the frequency, τ is the transmittance, p_s is the surface pressure, p is the pressure at a particular height, and T_s is the surface skin temperature.

The MSU is a space-borne microwave radiometer flown onboard the TIROS-N series of polar orbiting satellites operated by the National Oceanic and Atmospheric Administration (NOAA). It has four spectral channels in the 50 to 58 GHz O_2 absorption band (Smith et al., 1979). The 54.96 GHz, MSU channel 3, is the most sensitive to variations in the upper-tropospheric/lower-stratospheric thermal field (Velden, 1992). A typical weighting function shown in Fig. 2.3 reveals that the radiance measurements of this channel represent a broad layer average brightness temperature, with peak response in the 400-100-mb layer. Attenuation of the signal from cloud and precipitation is minimal since hydrometeors at this upper level are mainly in ice form that have little effect on outgoing radiation at 54.96 GHz. Therefore, channel 3 is ideal for observing thermal structure in cloudy regions associated with extratropical cyclones (Velden, 1992).

C. PARKE'S STUDY

1. Six-month Data Set

Global MSU brightness temperature data for the period 01 October 1993 to 31 March 1994 as recorded by NOAA-11 and NOAA-12 were obtained from the Marshall Space Flight Center by Parke (1994). From this data set, satellite passes between 25° N and 65° N and within 1.5 hours either side of 0000 UTC and 1200 UTC were extracted. A bias of approximately 2K between the two satellites (NOAA-12 warmer than NOAA-11) was corrected by applying a latitudinally-smoothed offset to the NOAA-12 data. Parke then used a multi-quadric interpolation scheme (Nuss and Titley, 1994) to objectively analyze the approximately 110 km resolution brightness temperature data on a regular 2.5° latitude by 2.5° longitude (145 by 17) grid centered at 45° N, 180° W for each map time.

Corresponding 12-h conventional analyses of numerous fields were obtained from the National Meteorological Center's Global Data Assimilation System (GDAS) at all mandatory levels. From these, derived fields of vorticity, potential vorticity, dynamic tropopause and thickness were calculated. Table 2.1 is a complete list of these fields.

2. Summary of Results

Parke (1994) concentrated on the correlations between the MSU channel 3 brightness temperatures and several of the conventionally derived fields: 400-100-mb thickness, 50-mb

1. Sea-level Pressure (mb)
2. 1000 - 500 mb Thickness (mb)
3. 400 - 100 mb Thickness (mb)
4. 250 mb Temperature (K)
5. 200 mb Temperature (K)
6. 500 mb Height (Dm)
7. 400 mb Height (Dm)
8. 100 mb Height (Dm)
9. 50 mb Height (Dm)
10. 500 mb Vorticity (10^{-5} s^{-1})
11. 100 mb Vorticity (10^{-5} s^{-1})
12. 300 mb Isentropic Pot. Vorticity (10^{-6} m^2 s^{-1} K kg^{-1})
13. Dynamic Tropopause (1.5 x 10 m^{-6} s^{-1} K kg^{-1})

Table 2.1. Conventional fields obtained from the National Meteorological Center's GDAS. From Parke (1994).

heights, 500-mb heights, 50-mb vorticity, dynamic tropopause, 200-mb temperatures and sea-level pressure. He found the spatial and temporal correlations for most of these fields associated with developing baroclinic waves to be consistent with the hydrostatic arguments discussed by Hirschberg and Fritsch (1993). In this thesis, we concentrate and expand upon Parke's discussion of the MSU-400-100-mb thickness, 500-mb height and 50-mb height correlations because these have direct forecasting implications.

a. Temporal Correlations

Parke (1994) calculated temporal correlation coefficients between MSU channel 3 data and the conventional fields at grid point locations by first normalizing the channel 3 MSU brightness temperatures and conventional data and then performing the following operation:

$$\rho_{i,j} = \rho(m,c)_{i,j} = \frac{Cov(m,c)}{\sqrt{V(m)V(c)}}, \tag{2.2}$$

where $\rho_{i,j}$ is the temporal correlation coefficient between the brightness temperature (m) and the conventional data (c) series of interest at grid point i,j, Cov is the covariance and V is the variance. Scale dependencies were investigated using high-pass and low-pass elliptical filters applied to the time series at each point. Using time scales agreeing with classification schemes developed by Orlanski (1975) and Fujita (1986), wave periods producing synoptic-scale filtered series (shorter than 5 days) and longer than synoptic-scale filtered series (longer than 14 days) were used. A student's T-test was used to verify that the correlations were statistically significant.

As expected, the MSU channel 3 brightness temperature and 400-100-mb thickness temporal correlations in Parke's study showed high positive correlations over the entire global domain for all wavelengths. The low-pass filtered analyses, which responded mostly to long wave patterns showed the highest positive correlations, with values consistently increasing towards higher latitudes. The high-pass filtered analyses, while still highly positive, differed

in that the highest correlations were roughly along the climatological storm tracks over both the Eastern and Western Hemispheres.

The MSU-50-mb height correlations showed the highest positive correlations in the low-pass filtered data. The unfiltered data also exhibited high positive correlations, but the MSU-50-mb height correlations decreased dramatically for the high-pass filtered data. There was little correlation found between the MSU and the 500-mb heights in either the low-pass filtered or the unfiltered data. Conversely, the MSU-500-mb height correlations showed the highest negative correlations in the high-pass filtered data (Fig. 2.4), except for the Tibetan Plateau region, where the data was thought to be contaminated by surface data. These findings supported the scale findings discussed earlier, suggesting that large-scale thermal anomalies are spread upwards, while smaller scale anomalies are reflected downwards.

b. Spatial Correlations

Parke (1994) also divided the data into eight 30° by 30° sub-domains (Fig. 2.5) in which spatial correlation coefficients between brightness temperature and the conventional analysis fields were calculated for every 12-h map time. Scale dependencies in the correlations were also investigated. The sub-domains, which measure 2400 km by 3300 km, provided a natural filter for synoptic scale features once the latitudinal and longitudinal trends were removed from the data. This spatial-scale separation of the data was accomplished following the method of Errico (1985). Larger than synoptic-scale waves were removed by first computing the slope of the surface for each j by

$$s_j = \frac{a_{N_I j} - a_{1j}}{N_I - 1} \quad , \tag{2.3}$$

where s_j is the slope of the j^{th} longitude and N_I is the maximum width of the sub-domain. Next the trend in the i direction was removed for each i,j through

$$a'_{ij} = a_{ij} - \frac{1}{2}(2i - N_I + 1)s_j \quad , \tag{2.4}$$

where a'_{ij} is the grid point detrended in the longitudinal direction. Finally, reversing i,j detrends the data in the latitudinal direction, with a'_{ij} in equation (2.4) replacing a_{ij} in equation (2.3) and results in a two-dimensionally "detrended" field that is periodic with wavelengths less than or equal to the domain size. As will be stressed later, this method is limited by the fact that it removes linear trends only. The "trended" portion of the analysis representing the large-scale features was obtained by subtracting the detrended fields from the full analysis.

Spatial correlation coefficients were compiled for the full, trended and detrended analyses for each field and calculated with

$$\rho_a = \rho(m,c) = \frac{Cov(m,c)}{\sqrt{V(m)V(c)}} \quad , \tag{2.5}$$

where ρ_a is the area correlation coefficient, *Cov(m,c)* is the covariance of the MSU data and conventionally derived data at each grid point *i,j* for each map time, and *V(m), V(c)* are the variances of the MSU data and conventional data over the sub-domain. Prior to the calculation of the correlation coefficients, the data was normalized by removing the sub-domain mean from the fields. Six-month average correlations were determined for each sub-domain by adding the total 12-h coefficients over the six months and dividing by the total number of analysis times.

Parke (1994) performed one further separation of the data by grouping times according to the correlation between the MSU and the 400-100-mb thickness values. Since the channel 3 MSU brightness temperature is most directly related to the thickness of this layer, as seen by the weighting function in Fig 2.3, a correlation of ≥ 0.80 was considered a viable analysis, while a correlation of < 0.80 was taken to indicate a potentially corrupted analysis that would make all subsequent correlations suspect. Therefore, times with an MSU - 400-100-mb correlation of < 0.80 were discarded and not considered in the viable or "good" data set.

Table 2.2 shows the six-month average results from Parke (1994) for each sub-domain and field that we are going to focus on in this study. These results generally show consistent and readily explainable correlations similar to the temporal results, suggesting the use of MSU data as a forecasting aid. However, some specific questions about the spatial results were left unanswered by Parke. The first is the large-scale trend MSU-50-mb height correlations over the Western Hemisphere (sub-domains 5 - 8). It was believed that these should have been highly positively correlated, similar to the temporal findings and the spatial

findings over the Eastern Hemisphere. The low correlations that were actually obtained need to be explained.

SUB-DOMAIN	MSU-400-100-mb thickness TOTAL FIELD	MSU-50 mb TREND	MSU-500 mb DETREND
1	0.86	0.87	-0.58
2	0.89	0.91	-0.56
3	0.90	0.90	-0.52
4	0.92	0.78	-0.79
5	0.88	0.01	-0.84
6	0.88	0.08	-0.78
7	0.86	0.24	-0.70
8	0.84	0.22	-0.63

Table 2.2. Six-month average spatial correlations between the total MSU and 400-100-mb thickness, trend MSU and 50-mb height, and detrend MSU and 500-mb height fields obtained by Parke (1994)for the eight sub-domains (Fig. 2.5).

There are also problems in the small-scale detrended MSU-500 mb data set. Although the average correlations are highly negative in each area, there were times during the six months when the correlations were unexpected. For example, there were four periods of time out of the 354 map times in sub-domain 6 (western United States and Canada) where the correlation was near zero or even positive (Fig. 2.6). To use the MSU analysis as a forecasting aid, these periods of questionable correlations need to be more fully understood. Therefore, following the recommendations of Parke (1994) and using the methods described in the next chapter, we investigate these problems.

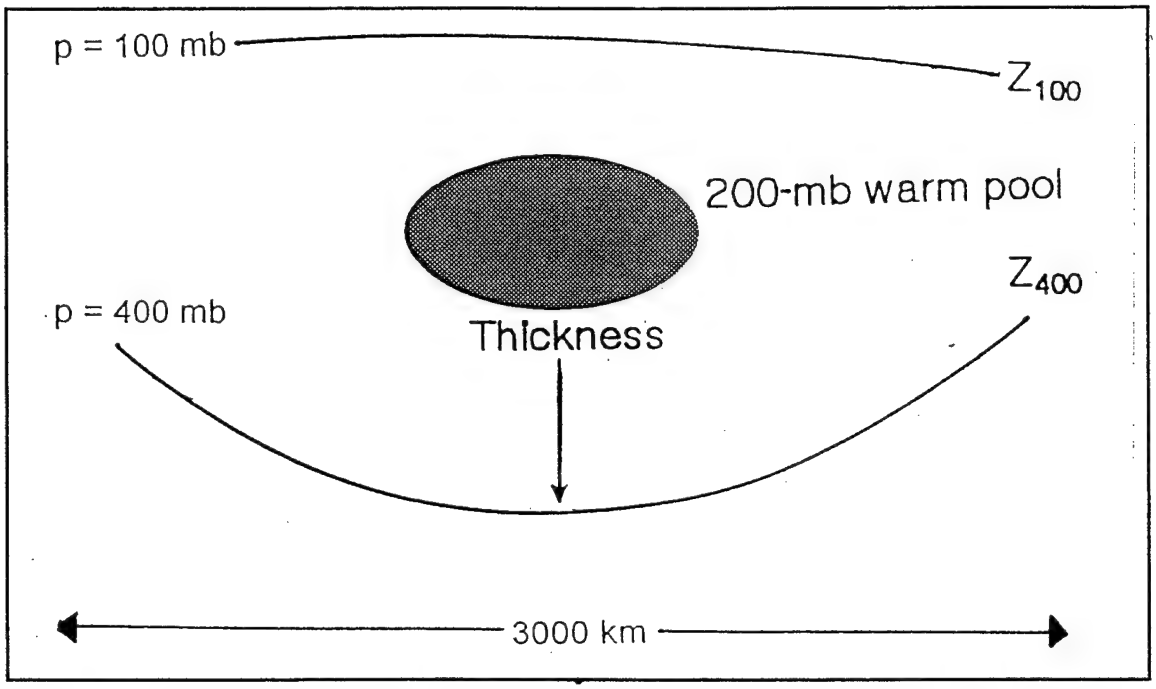

Figure 2.1. Conceptual diagram of the effects of synoptic-scale warming in the 400-100-mb layer.

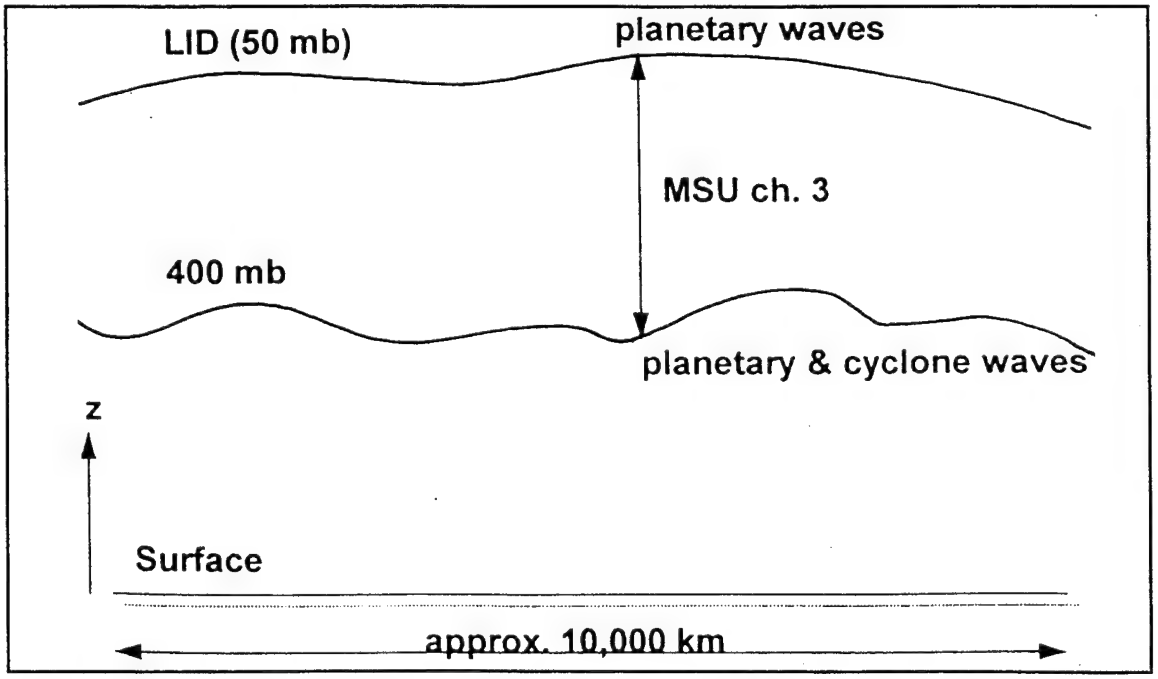

Figure 2.2. Conceptual diagram of wave structures on the 400-mb and 50-mb height surfaces. The thermal structure of the layer is measured by MSU channel 3. From Spencer et al., (1995).

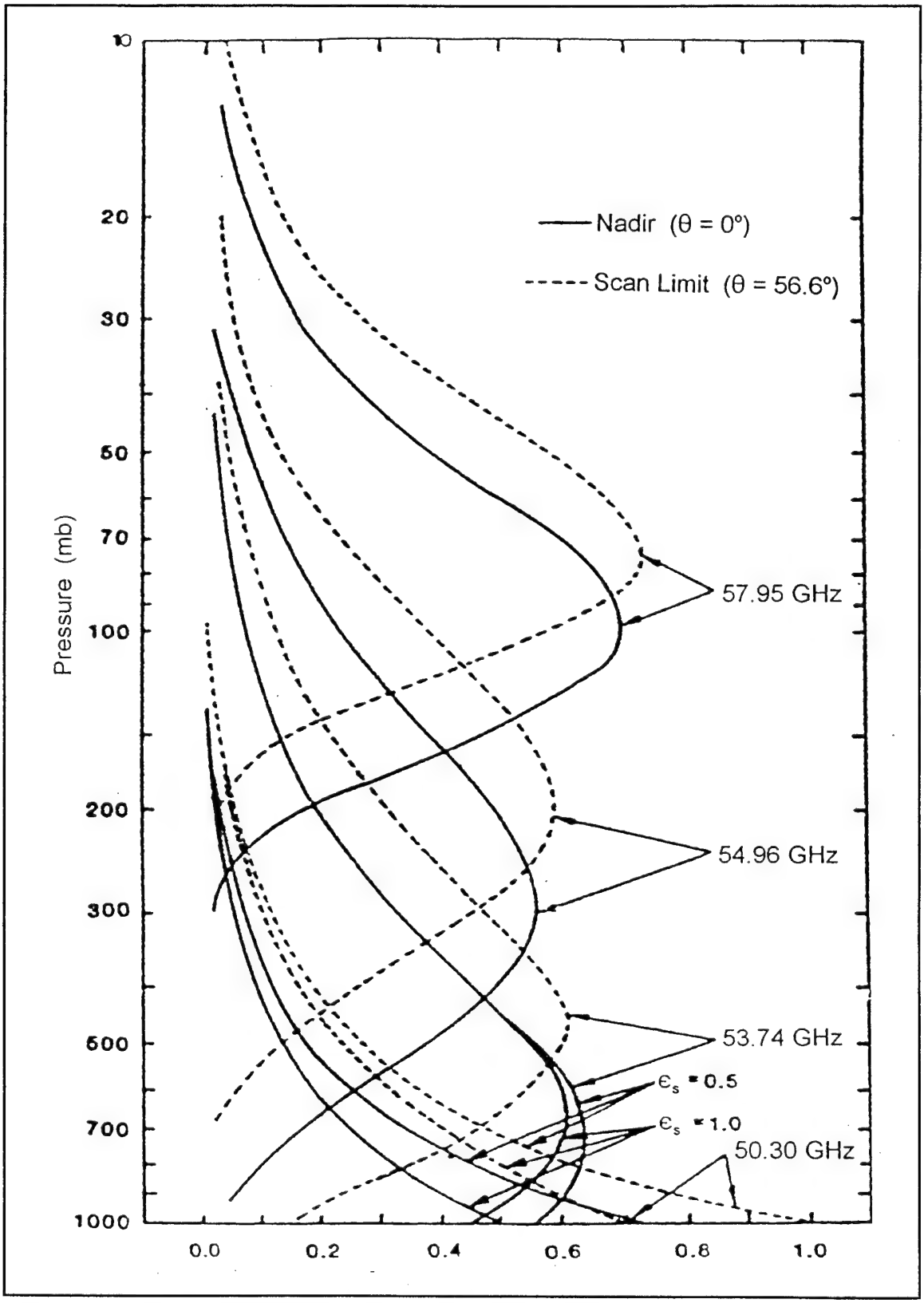

Figure 2.3. MSU weighting functions. From Grody (1983).

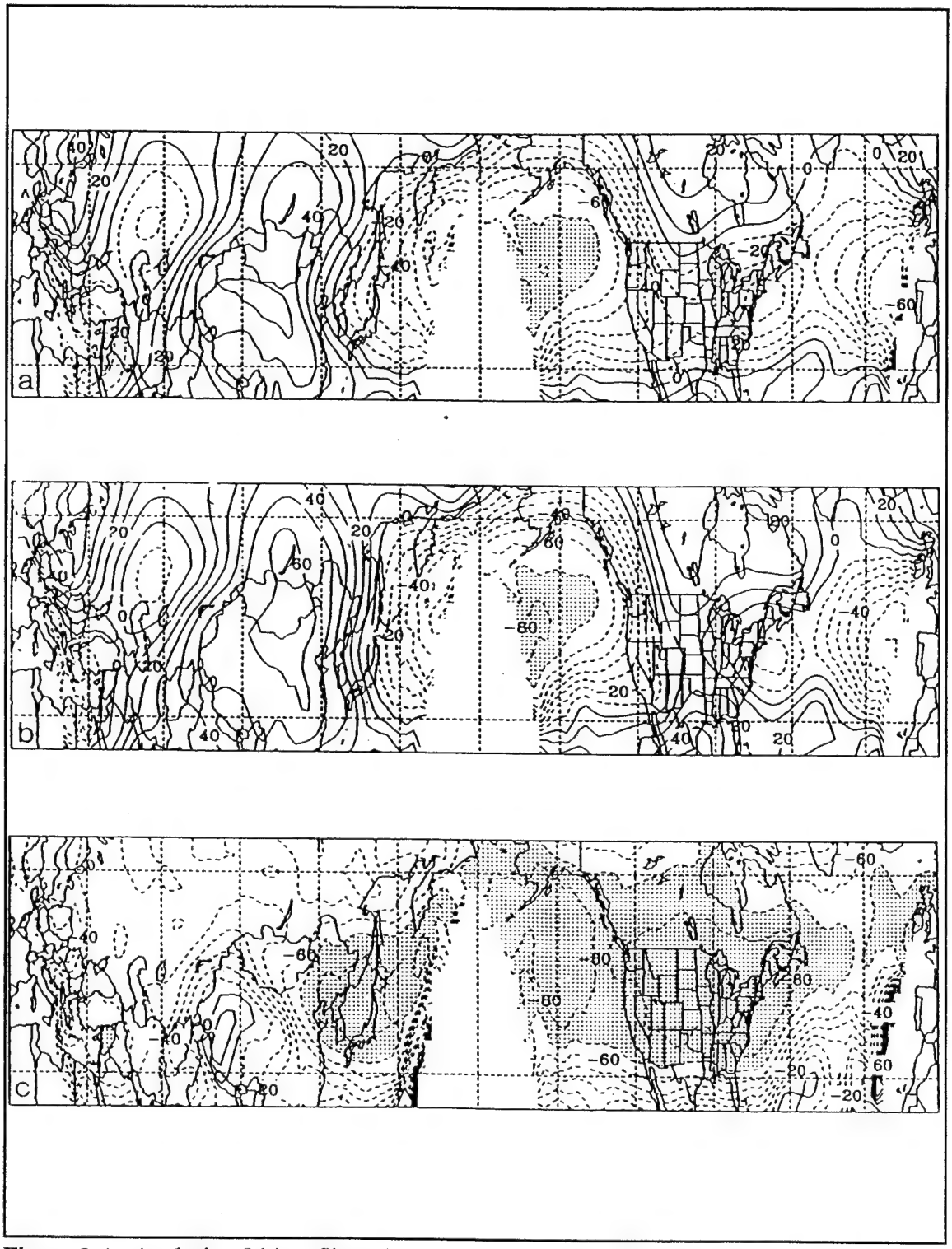

Figure 2.4. Analysis of (a) unfiltered, (b) 14 day low-pass filtered, and (c) ≤ 5 day high-pass filtered six-month temporal correlation coefficients (solid, contour interval 10^{-2}) between the channel 3 MSU and 500-mb heights. Light (dark) stippling represents correlations ≥ 0.70 (≥ 0.90). From Parke (1994).

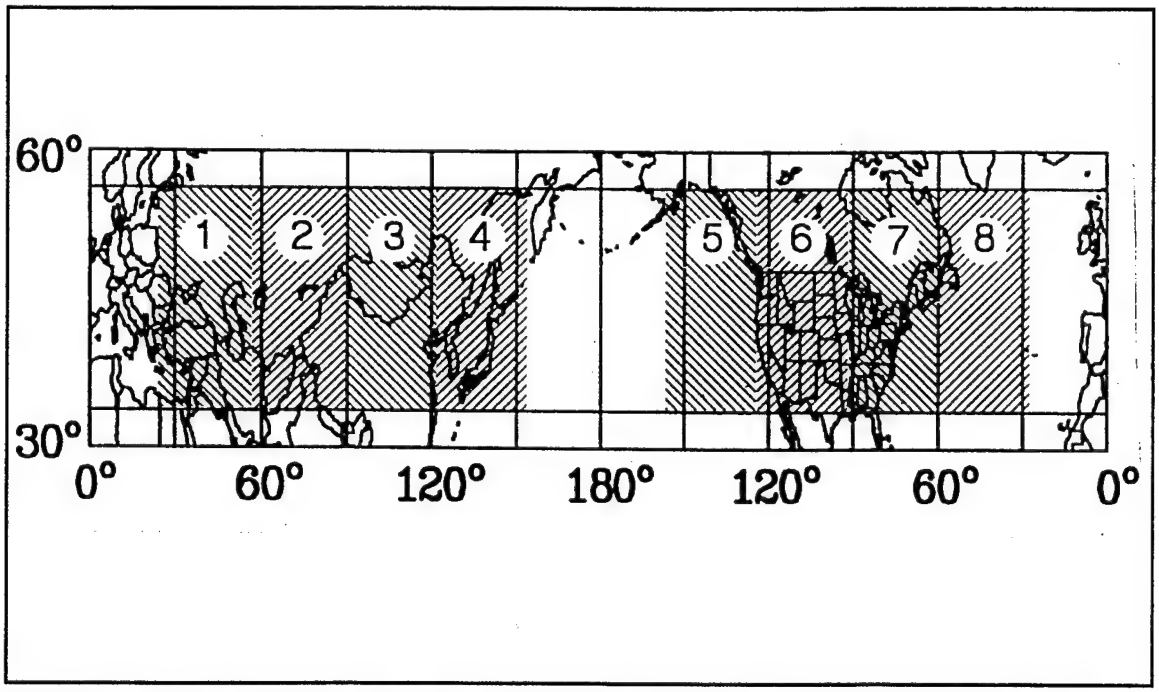

Figure 2.5. Map of the sub-domains used in the calculation of spatial correlations for each map time between the channel 3 MSU brightness temperature and various conventionally-derived fields. Stippled regions with numbers indicate the eight sub-domains over which the spatial correlations were calculated. From Parke (1994).

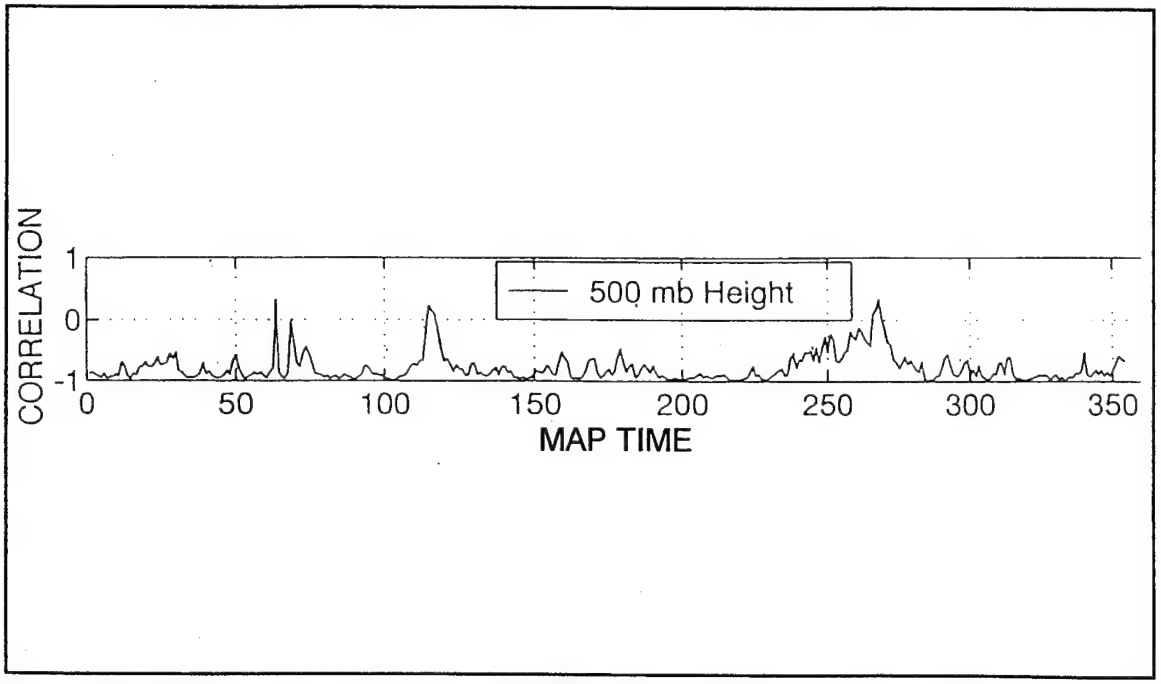

Figure 2.6. Individual map time detrend MSU-500-mb height correlations for sub-domain 6 from 01 October 1993 to 31 March 1994. From Parke (1994).

III. RESULTS

To expand and clarify the results in Parke (1994), it was necessary to more closely examine the synoptic characteristics of the atmosphere and the spatial correlations for each of the 364 map times during the six month period. Specifically, the 50-mb height, 500-mb height and MSU brightness temperature analyses were examined along with the trended MSU-50-mb and detrended MSU-500-mb correlations for each sub-domain and for every time.

As Parke (1994) suggests, one potential source of varying MSU-height correlations is that these correlations may change with synoptic regime. Hence, the first step was to visually check the analyses for obvious patterns that corresponded to unexpected correlation times. This visual inspection indicated that the correlations may have been sensitive to the strength of the zonal gradient, with the correlations between the MSU and the 50-mb trend and 500-mb detrend height field weakening as the westerlies intensified. These correlations also appeared to weaken when barotropic conditions existed at the upper levels.

Unfortunately, an attempt to quantify this subjective finding proved to be inconclusive. It was hypothesized that a zonal index could be used to stratify the six-month data set into specific synoptic regimes. A correlation between the zonal index and the MSU height correlations could theoretically identify synoptic regimes that led to high correlations and those that led to low correlations. In particular, a thermal wind zonal index value for each sub-domain was calculated by using the u-component of the thermal wind between 400 mb and 100 mb given by

$$U_T = U_{g_{100}} - U_{g_{400}} = -\frac{g}{f}\frac{\partial}{\partial y}[Z_{100} - Z_{400}] = -\frac{R_d}{f}\ln\left(\frac{p_{400}}{p_{100}}\right)\frac{\partial T_v}{\partial y}, \quad (3.1)$$

where the mean virtual temperature gradient is taken between 55° N and 35° N. As is the case with the conventional zonal index defined in terms of the 500-mb meridional height gradient or zonal geostrophic wind, high thermal index values or high zonal thermal wind speeds indicate less wave activity in the 400-100-mb layer.

Table 3.1 shows the results for the detrended MSU-500-mb height correlations for sub-domains 2 and 7 and the trend MSU-50-mb height correlations for the Eastern (sub-domains 1-4) and Western (sub-domains 5-8) Hemispheres. Although no strong correlations are evident, it does appear that there is some utility in using this zonal index as a predictor of MSU utility when the 400-100-mb layer is mostly above the tropopause. That is, when the sheer in the layer is negative, and the north-south thermal gradient is positive. This observation is noted as an area for further research.

Another potential source of unexpected correlation may be the method by which the statistics are calculated. To gain a better understanding of the statistical procedure Parke (1994) used, four cases of the detrend MSU-500-mb height correlations (Fig. 2.5), one with an expected (high negative) correlation and three with unexpected (near zero or positive) correlations, were further examined. The analysis at 0000 UTC 22 Jan 1994 (map time 202) for sub-domain 6 was arbitrarily picked from the expected correlation times. Figure 3.1 shows the total 500-mb height field and the MSU brightness temperatures as would be seen

ZONAL INDEX - MSU-500-mb DETREND

SUB-DOMAIN	PERIOD	AVERAGE ZONAL INDEX	CORRELATION
2	OCT - DEC	5.52	0.32
	JAN - MAR	6.84	0.55
7	OCT - DEC	-3.65	0.75
	JAN - MAR	-0.80	0.79

ZONAL INDEX - MSU-50 -mb TREND

EAST HEM	OCT - DEC	5.41	0.44
	JAN - MAR	6.13	0.24
WEST HEM	OCT - DEC	-2.68	0.54
	JAN - MAR	-2.24	0.66

Table 3.1. Three-month average correlations between the thermal wind zonal index and the detrend MSU-500-mb and the trend MSU-50-mb height correlations for sub-domains 2 and 7 and the Eastern and Western Hemispheres respectively.

by an operational forecaster. There is an MSU brightness temperature minimum associated with a pronounced 500-mb ridge, which indicates a strong negative correlation. The detrended field charts (Fig. 3.2) show a dominant, nearly circular 400-100-mb thickness minimum, MSU temperature minimum and 500-mb height ridge. Not surprisingly, the detrend correlation coefficient for this particular time was -0.98.

The high negative correlation notwithstanding, the manner in which the average correlation coefficients were obtained was examined. Parke (1994) used Matlab, a statistical package (Janzow, 1992) to calculate the statistics. Each data field for the eight sub-domains,

which was arranged in a 13 by 13 point grid was converted by Matlab to a single 169 row column vector. Row one began at the southwestern most grid point. The vector was then built by moving eastward along the southernmost latitude circle to the southeast corner of the sub-domain. This was repeated for the next latitude circle up, and so on until the northern latitude circle was reached. The correlation coefficient for any two fields was then calculated by comparing two column vectors.

It was hypothesized that this "area correlation" method may not have been fair in describing the correlations that were apparent visually in various cases, especially in the east-west direction. To investigate this, the method of calculating the correlation coefficients was modified by first calculating separate correlation coefficients across each latitude circle and longitude meridian within a sub-domain, then averaging the 13 resultant coefficients to arrive at the sub-domain correlation coefficient. These latitude (longitude) correlations were believed to be better able to reveal the patterns in the east-west (north-south) directions.

Figure 3.3 shows the normalized MSU and 500-mb height values at each individual grid point in sub-domain 6 obtained by the latitude and longitude averaged method for this case. The latitude average correlation was computed as -0.72 and the longitude average correlation was -0.99. Therefore. the longitude correlation appears to dominate the area correlation. Notice the symmetry both east-west and north-south in the fields. For later comparison, also notice that there is no large-scale signal in the longitude correlations. In other words, there is no linear trend or some higher order quadratic trend in the north-south direction as we move west and east across the domain. There is however, a half-wavelength

signal present in the latitude correlations, which indicates a large-scale trend in the east-west direction as we move south and north. In this case, the half-wavelength signals in the MSU and 500-mb height correlations are negatively correlated.

The first example of an unexpected correlation time is at map time 70, corresponding to 1200 UTC 02 Nov 1993 for sub-domain 6. As can be seen in Fig. 3.4, there was a bad data point in the MSU field, evidenced by the erroneous bulls-eye in the southwest portion of the area. Unfortunately, this was not caught by the error check in the analysis program. This erroneous point led to a 0.43 correlation.

The second unexpected correlation case examined was the 0.34 detrended correlation near map time 270. The corresponding 500-mb height and MSU brightness temperature fields for 0000 UTC 16 Feb 1994 (Fig. 3.5) show again a 500-mb ridge associated with a general MSU temperature minimum although there is a smaller-scale wave present in the MSU analysis. Figure 3.6 shows the detrended MSU, 500-mb heights and 400-100-mb thickness fields for this time. A cold ridge evident in the MSU field appears to be aligned nicely with a large 500-mb ridge, indicating a negative correlation. Figure 3.7 shows the normalized correlations by latitude and longitude. As in the expected case, there is no apparent large-scale signal in the longitude correlation (Fig. 3.7b), which indicates consistency in the east-west direction. However, in this case the longitude correlations are positive (average = 0.44). Hence, though the average latitude correlation is negative (-0.35) as can be seen in Fig. 3.7a, there is a half-wavelength positively correlated signal as we move meridionally. It is this large-scale positive correlation that causes the overall correlation for the sub-domain to be positive. While the Errico detrending is intended to remove all

wavelengths greater than the area of the box, it is clear that it does not remove waves with half-wavelengths equal to the box size. These signals in the data may not be appropriate in the synoptic-scale correlations.

This case prompted an overall six-month comparison in the detrended fields of Parke's results with a latitude and longitude averaged correlation. This comparison is seen in Fig. 3.8 for sub-domain 6. Generally, the longitude-averaged method correlations (Fig. 3.8b) more closely resembles the area method results (Fig. 3.8a) of Parke (1994). In particular, times of poor (low negative and positive) correlation in Parke's results, between times 100 - 150 and 250 - 275 are reflected more in the meridional than the zonal direction.

Since this method of separating the data by latitude and longitude proved successful in revealing some problems with the detrending method, it was decided to recompute the six-month average correlations for each sub-domain. Table 3.2 shows the results of this. Even though the latitude-longitude method is useful in individual cases, it is apparent that the six-month average correlations using the area method yielded higher correlations compared to either the latitude or the longitude method.

The final example comes from sub-domain 7. As was the case for sub-domain 6, sub-domain 7 also shows that the MSU-detrended 500-mb height correlations are generally very highly negatively correlated (Fig. 3.9) over the six-month period. Map time 304 however, is one time when the correlation is strongly positive (0.60). Figure 3.10 shows the detrended MSU, 500-mb heights and 400-100-mb thickness fields for the corresponding time, 1200 UTC 10 March 1994. A prominent trough is present at 500 mb, just along the western border of the box. Using the latitude and longitude averaging method, there is a latitude

SUB-DOMAIN	AREA AVERAGE	LATITUDE AVERAGE	LONGITUDE AVERAGE
1	-0.58	-0.55	-0.49
2	-0.56	-0.44	-0.53
3	-0.52	-0.45	-0.49
4	-0.79	-0.61	-0.76
5	-0.84	-0.69	-0.80
6	-0.78	-0.75	-0.70
7	-0.70	-0.63	-0.65
8	-0.63	-0.59	-0.55

Table 3.2. Latitude and longitude averaged correlations compared with Parke (1994) area average correlations for MSU-500 mb detrend fields for the eight sub-domains.

average correlation of 0.08 and a longitude average correlation of 0.47. Once more, Fig. 3.11 shows a half-wavelength signal in the latitude method but no such signal in the longitude method.

In this case, it was hypothesized that the location of the prominent meteorological feature within the box may have something to do with the correlation value. Evidence for this lies in the fact that the 1200 UTC 11 March 1994 detrended fields (Fig 3.12) show the same meteorological pattern, only now more in the center of the box, and a corresponding correlation of -0.77.

To examine this hypothesis more fully, the box for sub-domain 7 was shifted for the 10 March data, placing the trough more in the center of the box (Fig. 3.13). As expected, the correlation improved to -0.88. Figure 3.14 shows the latitude and longitude average correlations. Because the Errico method produces a periodic signal within the box, it is

believed that features located near any of the four edges will be modified enough to give a misrepresentative correlation value.

Finally, we address the unexpected low positive spatial correlations Parke (1994) found between the trend (large-scale) MSU and the 50-mb heights over the Western Hemisphere (Table 2.2). Visual inspection of the 50-mb heights over the six-month period showed generally wavenumber one or two flow at this level, in agreement with climatology. Specifically, strong zonal or trough-like flow existed over the Eastern Hemisphere whereas the Western Hemisphere was more ridge-like. It was hypothesized that the unexpected correlations over the Western Hemisphere may have been the result of the combination of the invalidity of the thickness-spreading assumption (Hirschberg and Fritsch, 1993) near 50 mb during ridging conditions and the employment of the Errico (1985) scale-separation method over the eight relatively small sub-domains. Clearly the tropopause is higher in ridge conditions than in trough conditions, which would in turn enable tropospheric temperature anomalies to reach above 50 mb. This would invalidate Hirschberg and Fritschs' (1993) theory that argues for high positive MSU-50-mb height correlations for the large scales because their analysis is based on a model that confines thermal anomalies between two levels of interest, such as 100 mb and 400 mb. Unfortunately this potential problem with the thickness-spreading was difficult to access quantitatively in this study because the data only reached the 50-mb level.

Potential problems with the method of scale separation were a bit more tractable to investigate. In particular, it was speculated that the trend portion of the sub-domain boxes may have been contaminated by scales other than the large scales considered by Hirschberg

and Fritsch (1993) since the box sizes were only 2400 km by 3300 km.

To further investigate this, the size of the sub-domains was modified. Sub-domains 1 through 4 were combined into one big area, resulting in a 13 by 52 grid size. Similarly, sub-domains 5 through 8 were combined. These big areas measured 2400 km by 13200 km each, which enabled truer large-scale separation. Average correlation coefficients for MSU and each conventionally derived field were computed the same way as described above, with one additional step. Average correlations were done for three-month periods as well as for the six-month total average. It was speculated that there may have been a shift in the large scale weather pattern from the October to December period to the January to March period. Table 3.3 indicates that there was a marked positive shift of the Western Hemisphere correlations during the January through March 1994 period between the MSU-50-mb trend fields, which suggested more agreement with theory. Otherwise, the correlations were very similar.

In summary, many of the unexpected correlations in Parke (1994) were found to be the result of one of three issues; erroneous data, using an Eulerian area definition scheme or insufficient detrending using Errico (1985). Attempts to stratify data based on synoptic regime were inconclusive but some utility was found in using a thermal wind zonal index.

The next chapter will demonstrate real time use of MSU analysis fields by presenting two case studies.

SUB-DOMAIN	SIX MONTH	OCT - DEC	JAN - MAR
1	0.87	0.84	0.91
2	0.91	0.88	0.94
3	0.90	0.91	0.90
4	0.78	0.82	0.73
AVERAGE 1 - 4	0.88	0.86	0.88
5	0.01	-0.12	0.17
6	0.08	0.06	0.10
7	0.24	0.05	0.42
8	0.22	0.02	0.42
AVERAGE 5 - 8	0.14	0.01	0.27
EAST HEM	0.83	0.81	0.86
WEST HEM	0.36	0.21	0.51

Table 3.3. Comparison of Parke's (1994) original sub-domain and large sub-domain average trend MSU-50-mb height correlations over three- and six-month periods. Average 1-4 and 5-8 correlations are averages of Parke's sub-domains 1-4 and 5-8 correlations respectively. East Hem and West Hem are the large sub-domain correlations.

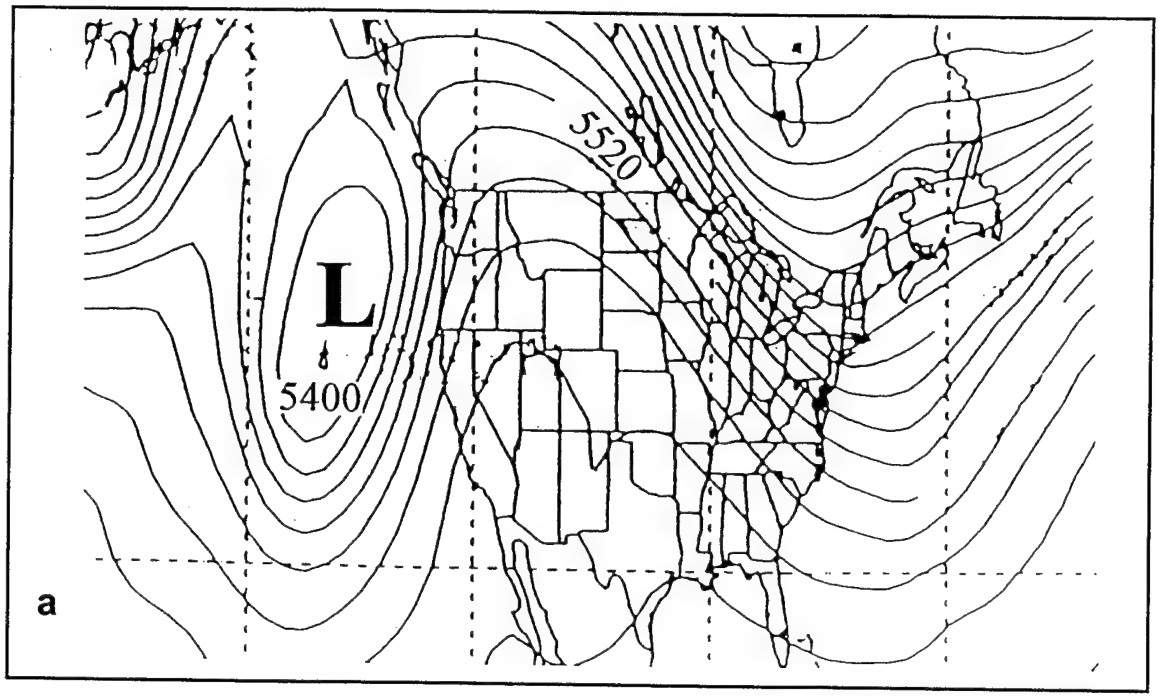

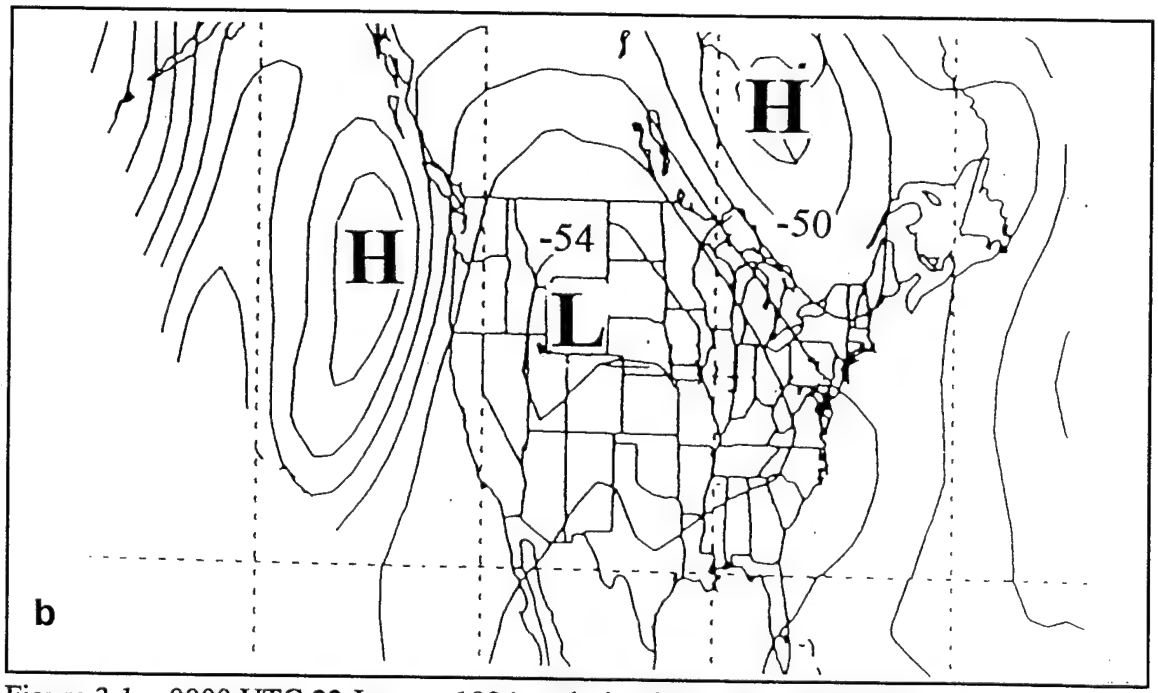

Figure 3.1. 0000 UTC 22 January 1994 analysis of (a) 500-mb height (contour interval is 60 m) and (b) channel 3 MSU brightness temperature (contour interval is 1 °C). In this and following figures "L"s and "H"s represent relatively low and high values, respectively.

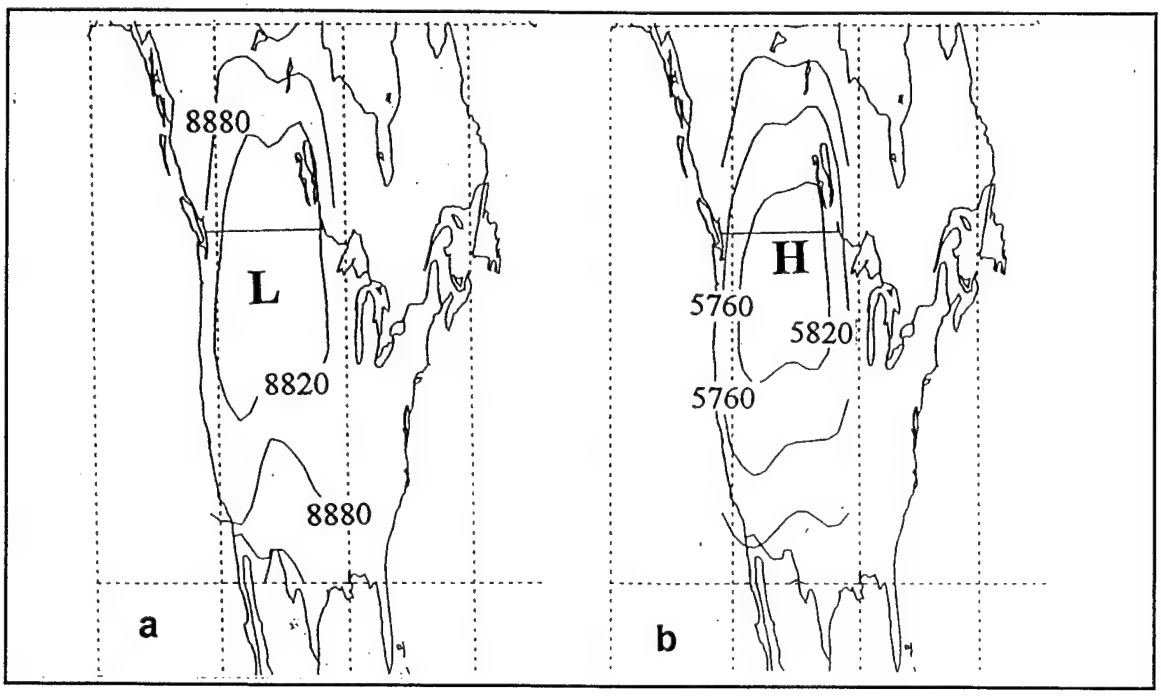

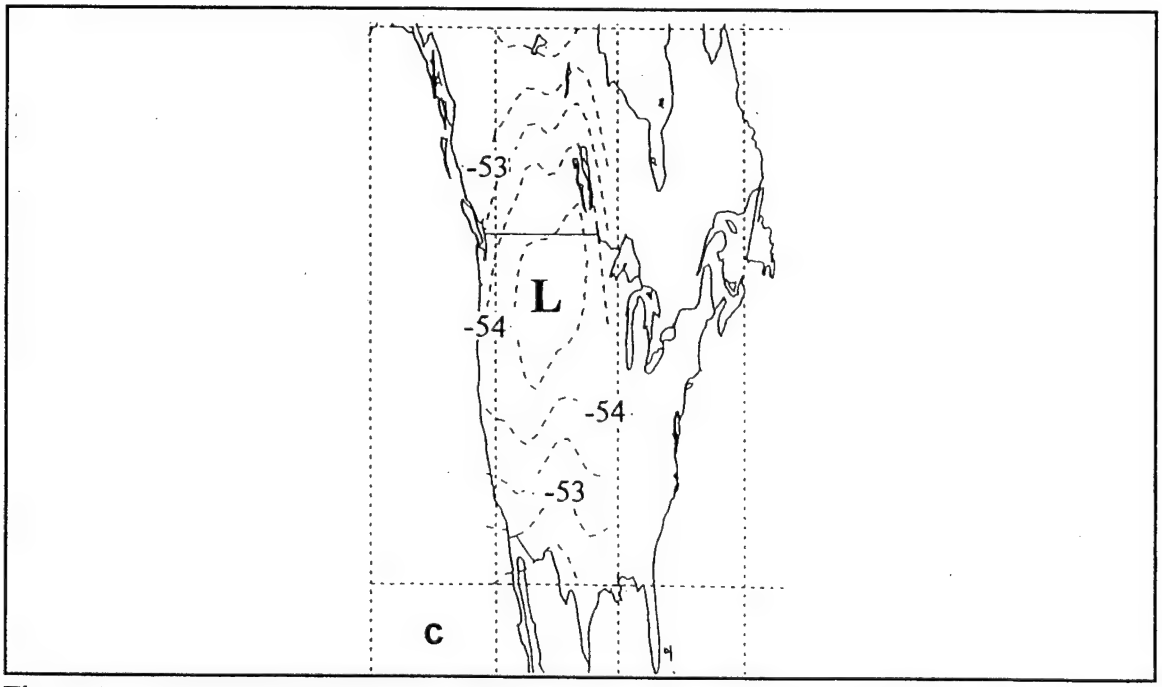

Figure 3.2. 0000 UTC 22 January 1994 analysis of detrended (a) 400-100-mb thickness (contour interval is 60 m), (b) 500-mb height (contour interval is 60 m), and (c) channel 3 MSU brightness temperature (contour interval is 1° C) for sub-domain 6.

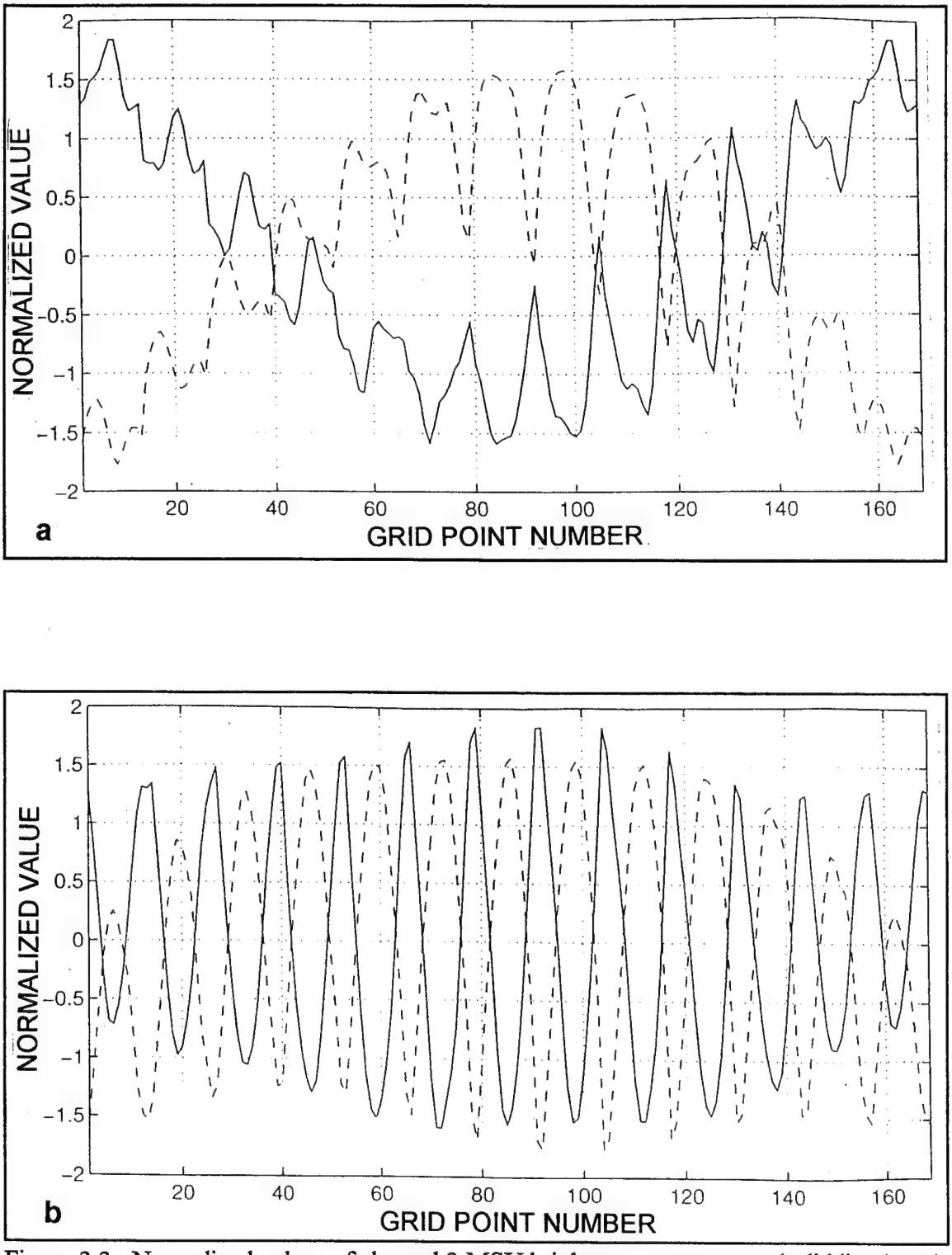

Figure 3.3. Normalized values of channel 3 MSU brightness temperature (solid lines) and 500-mb height (dashed lines) at each individual grid point in sub-domain 6 for the detrended 0000 UTC 22 January 1994 fields. Latitude method is depicted in (a), longitude method in (b).

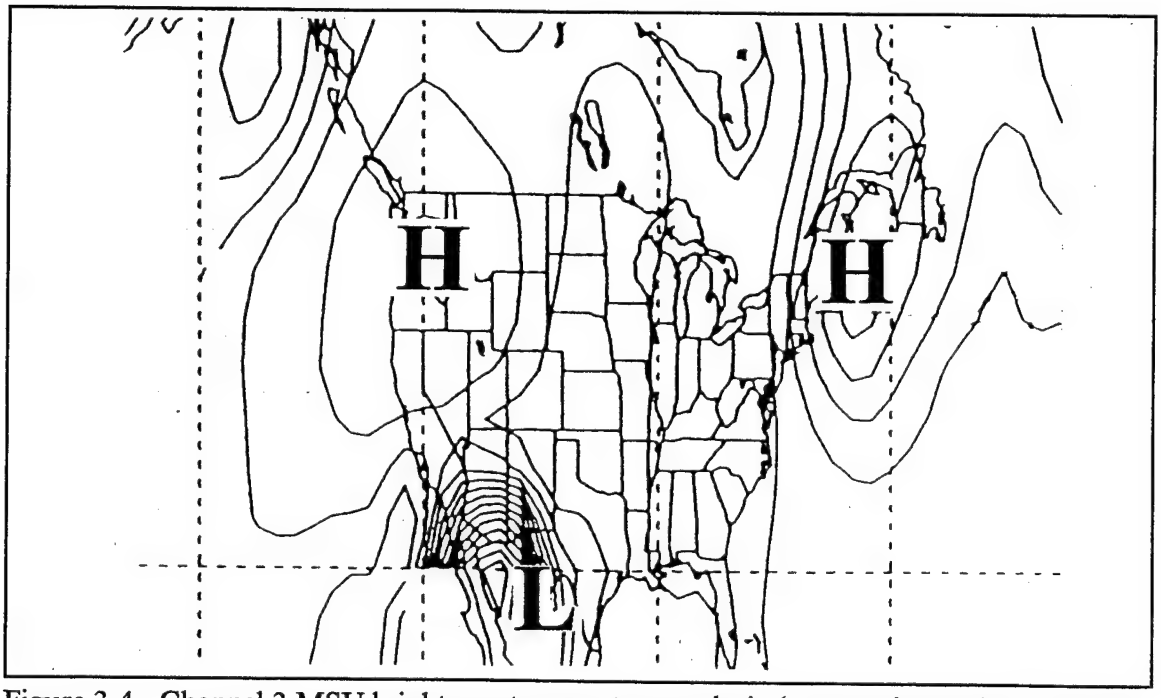

Figure 3.4. Channel 3 MSU brightness temperature analysis (contour interval is 1° C) for 0000 UTC 02 November 1993.

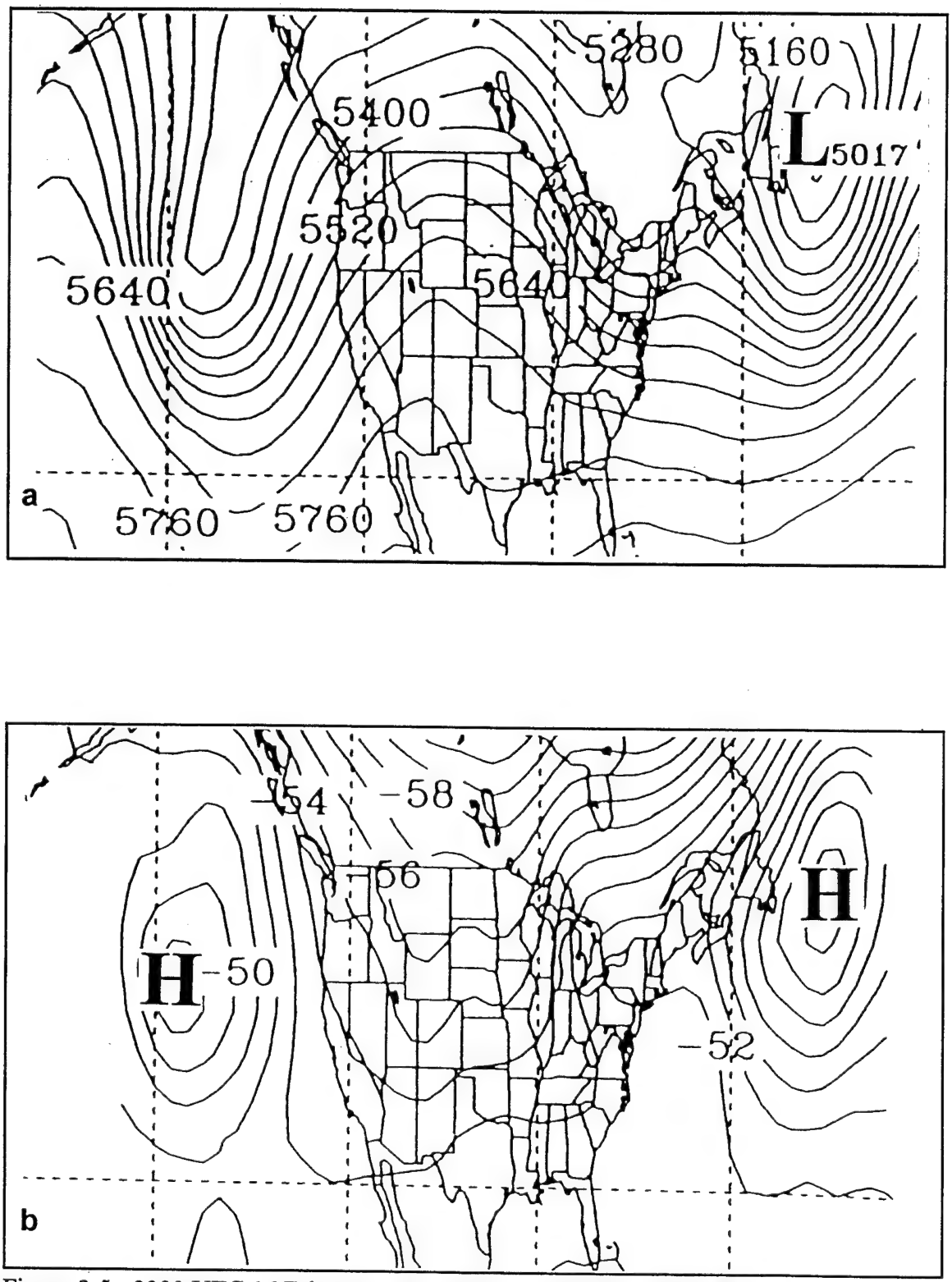

Figure 3.5. 0000 UTC 16 February 1994 analysis of (a) 500-mb height (contour interval is 60 m) and (b) channel 3 MSU brightness temperature (contour interval is 1° C).

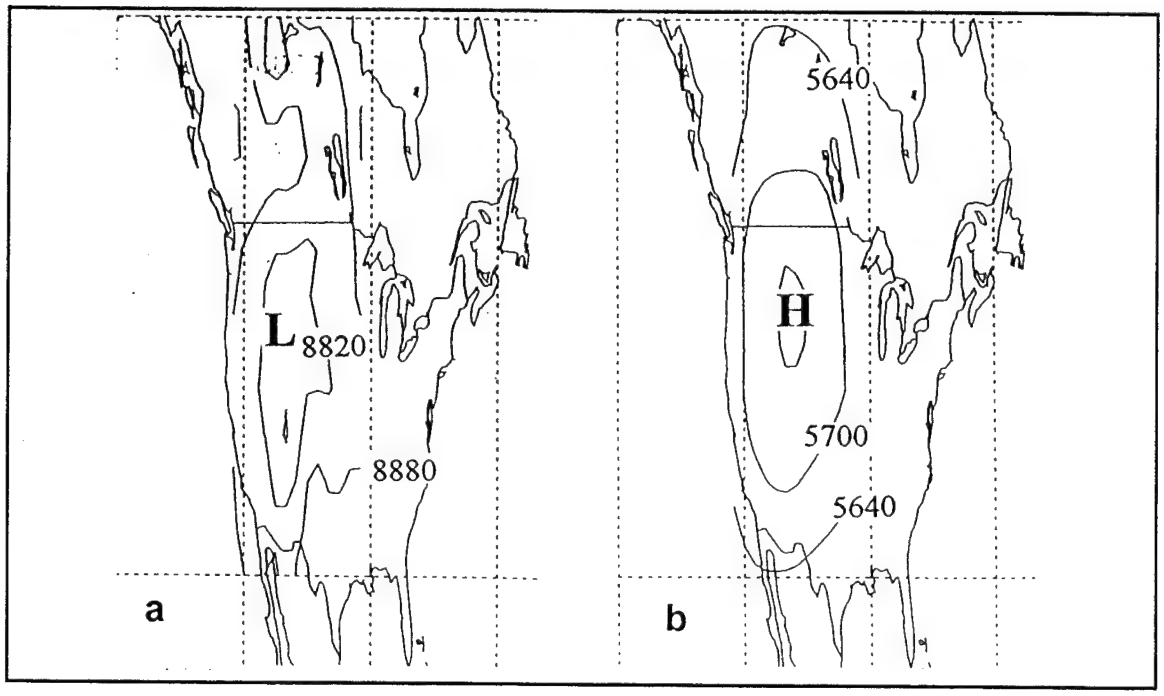

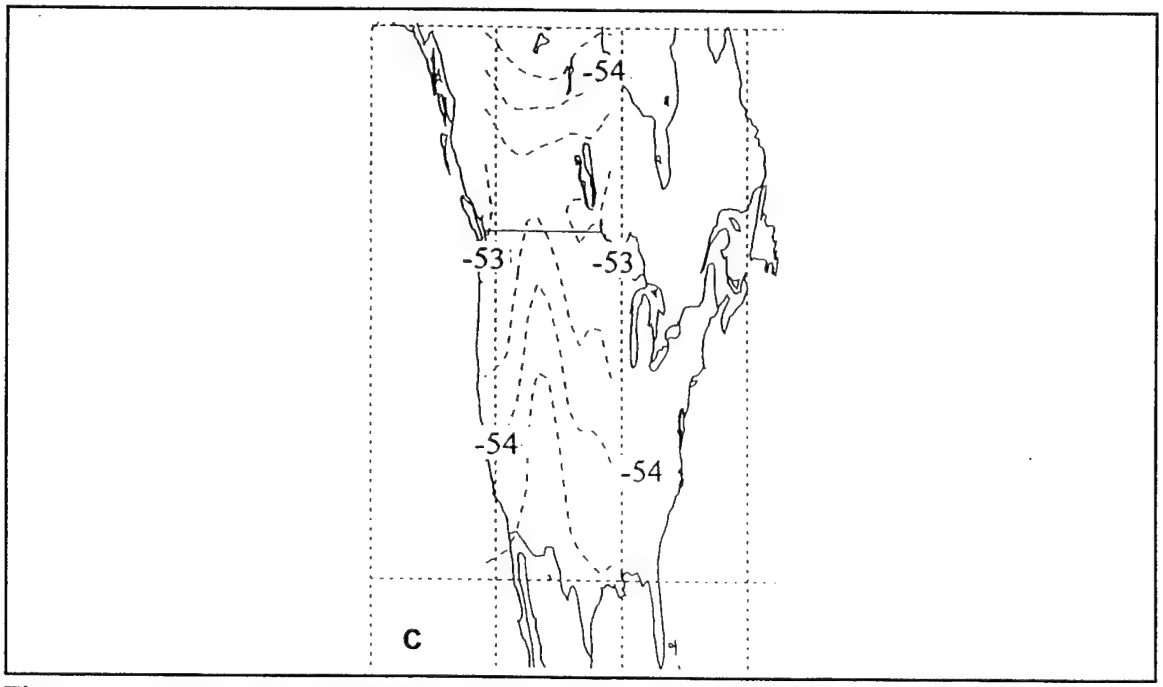

Figure 3.6. 0000 UTC 16 February 1994 analysis of detrended (a) 400-100-mb thickness (contour interval is 60 m), (b) 500-mb height (contour interval is 60 m), and (c) channel 3 MSU brightness temperature (contour interval is 1° C) for sub-domain 6.

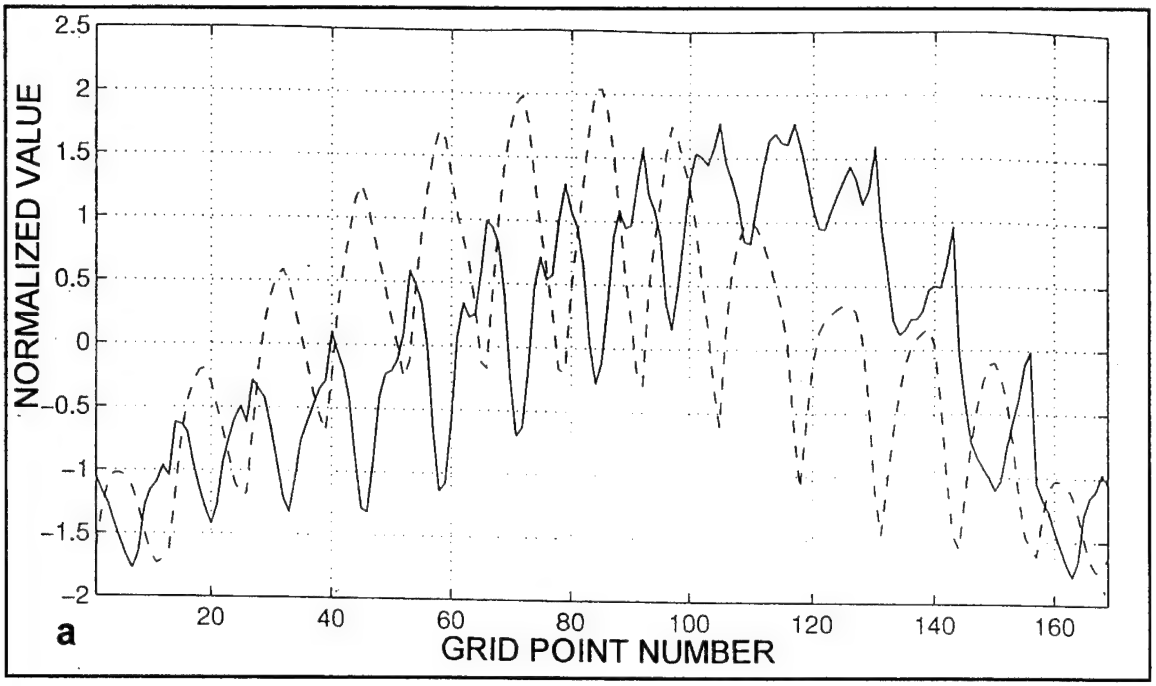

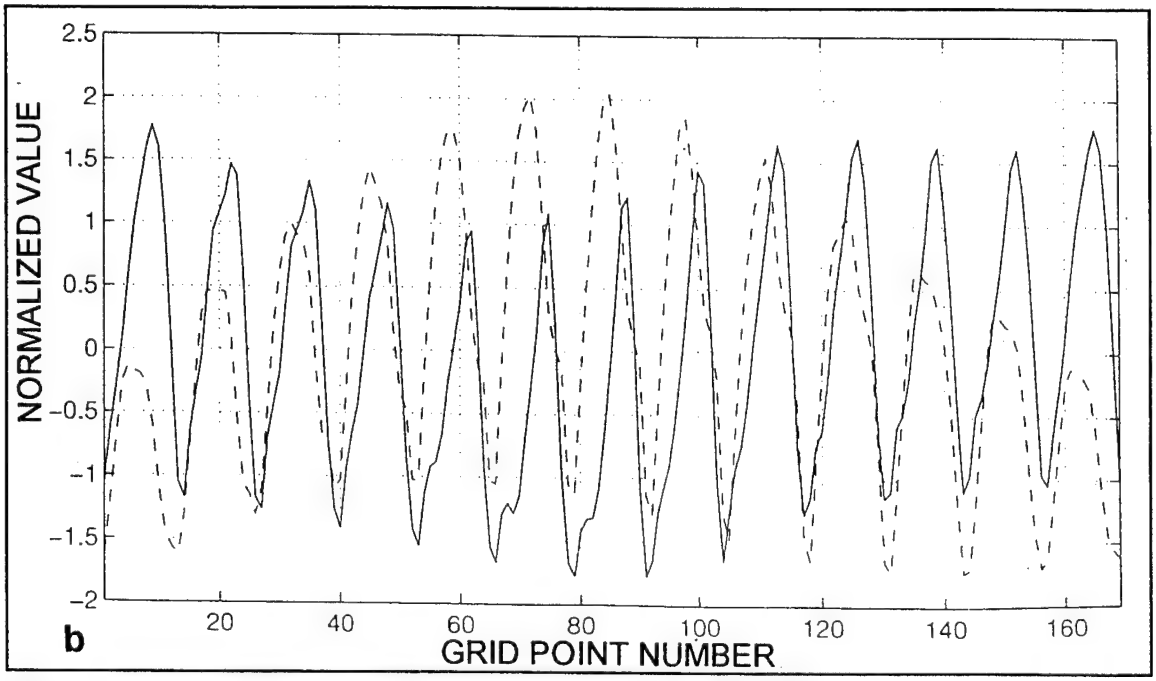

Figure 3.7. Normalized values for channel 3 MSU brightness temperature (solid lines) and 500-mb height (dashed lines) at each individual grid point in sub-domain 6 for the detrended 0000 UTC 16 February 1994 fields. Latitude method is depicted in (a), longitude method in (b).

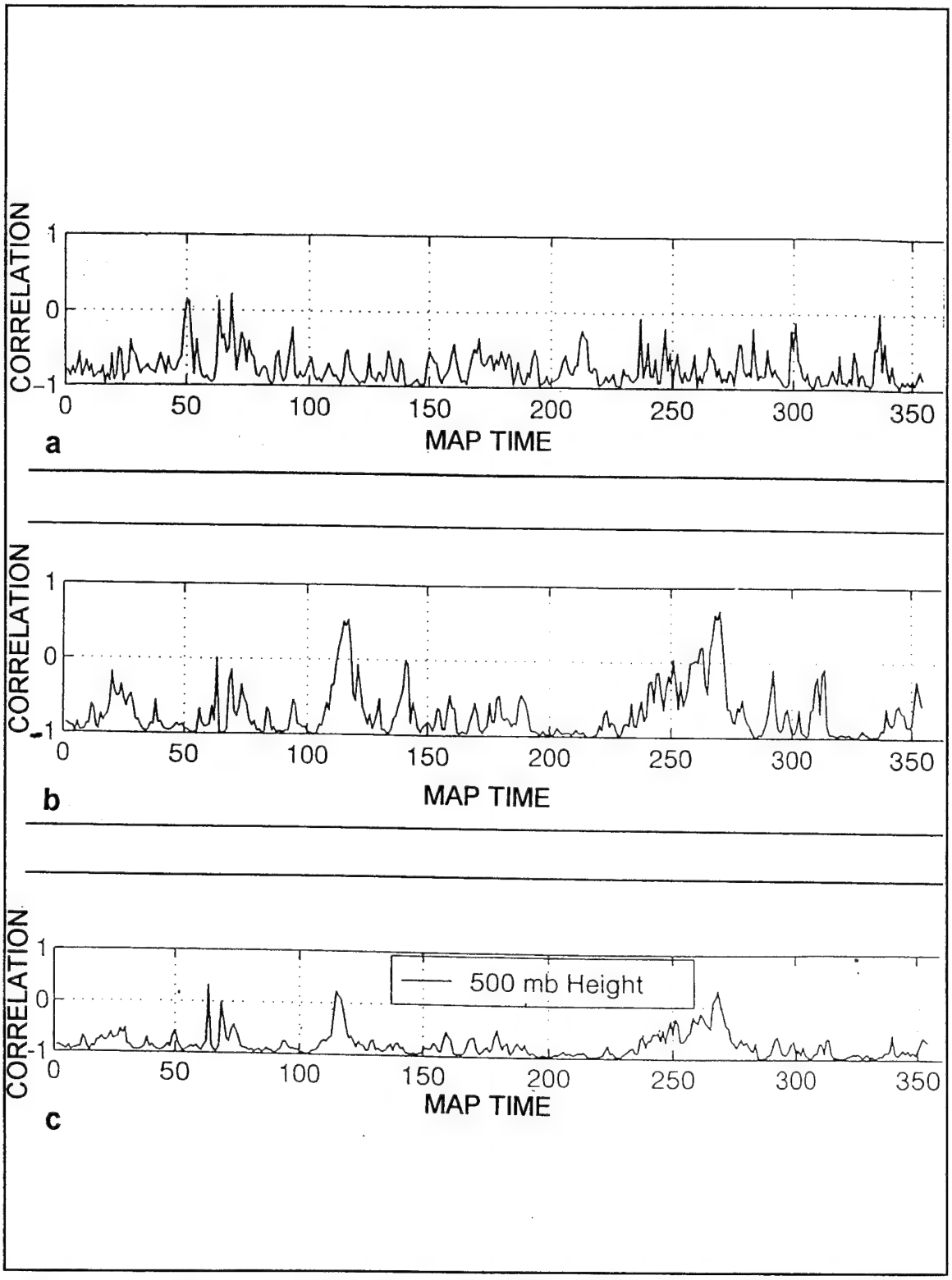

Figure 3.8. Comparison of individual map time detrend MSU-500-mb height correlations for sub-domain 6 as computed by (a) latitude average method, (b) longitude average method, and (c) Parke's area average method.

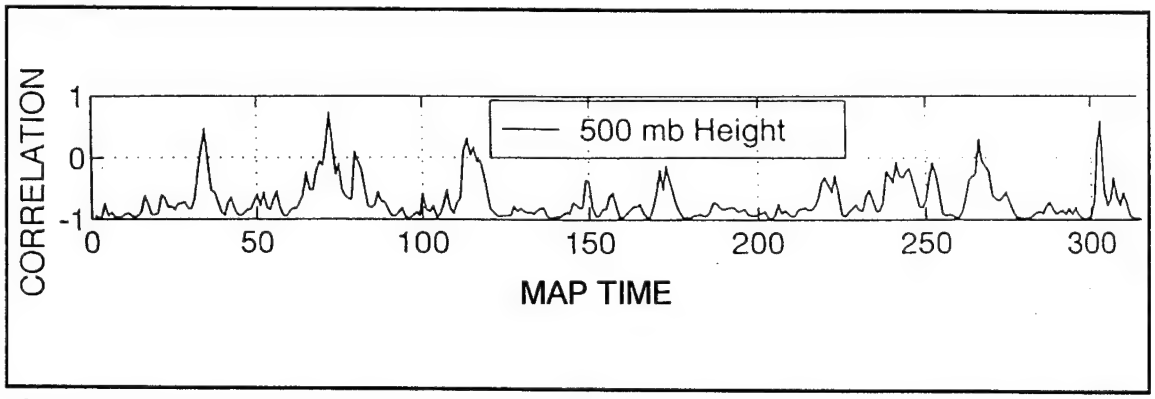

Figure 3.9. Individual map time detrend MSU-500-mb height correlations for sub-domain 7 from 01 October 1993 to 31 March 1994. From Parke (1994).

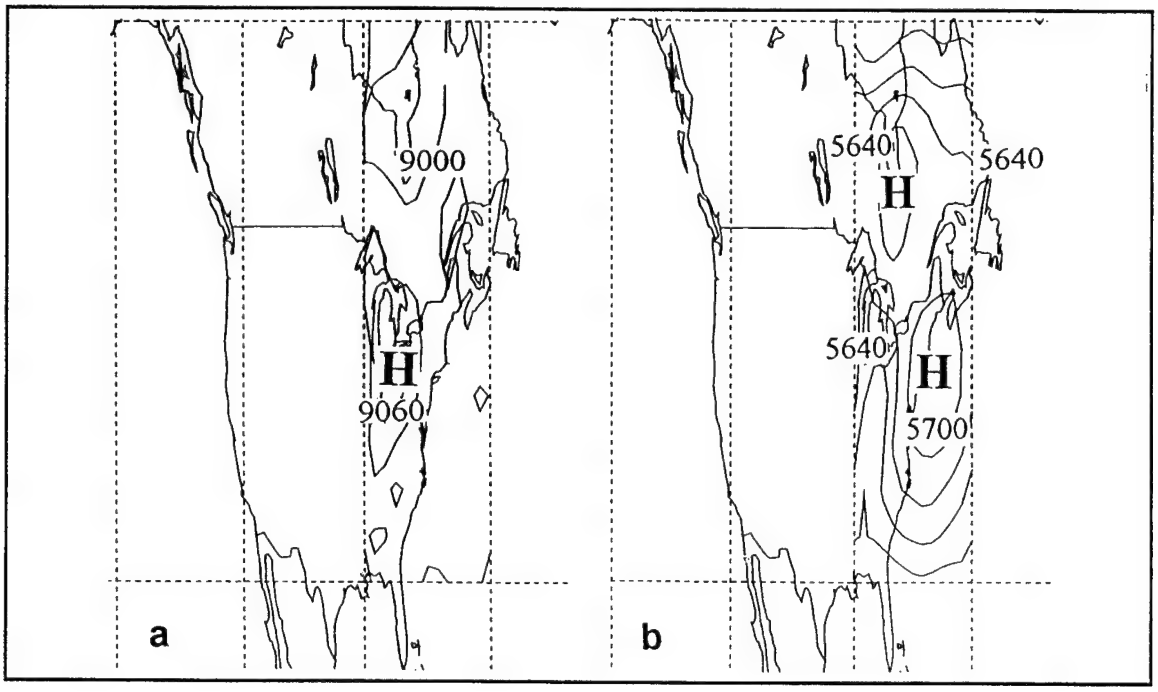

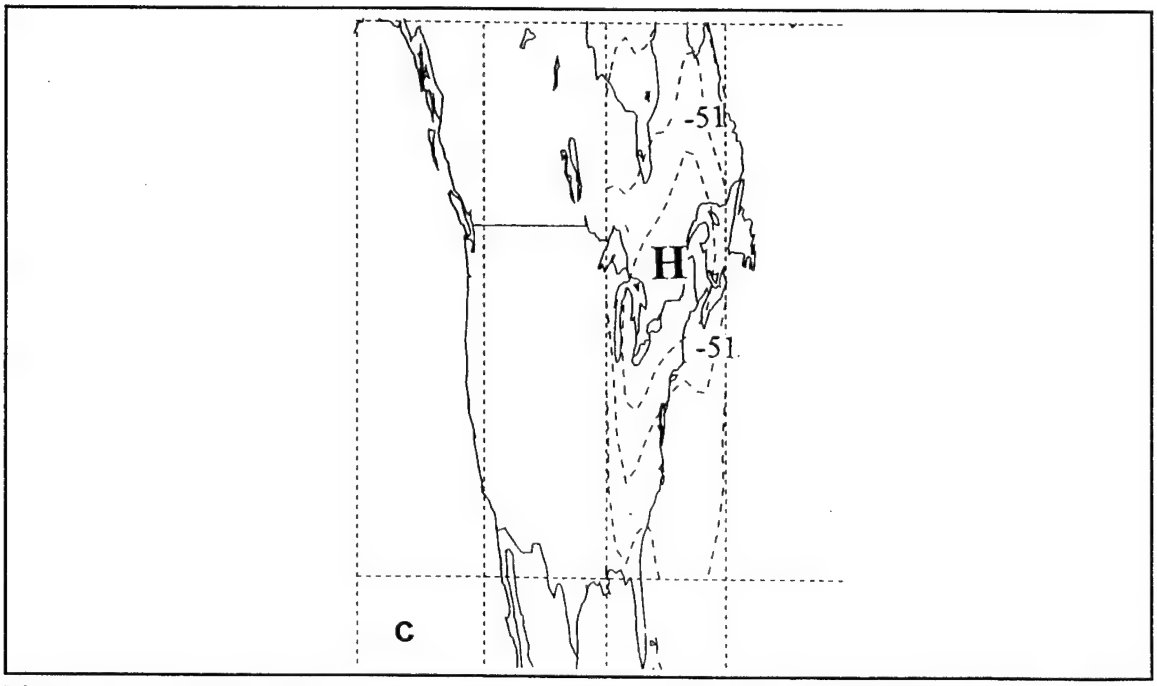

Figure 3.10. 1200 UTC 10 March 1994 analysis of detrended (a) 400-100-mb thickness (contour interval is 60 m), (b) 500-mb height (contour interval is 60 m), and (c) channel 3 MSU brightness temperature (contour interval is 1° C) for sub-domain 7.

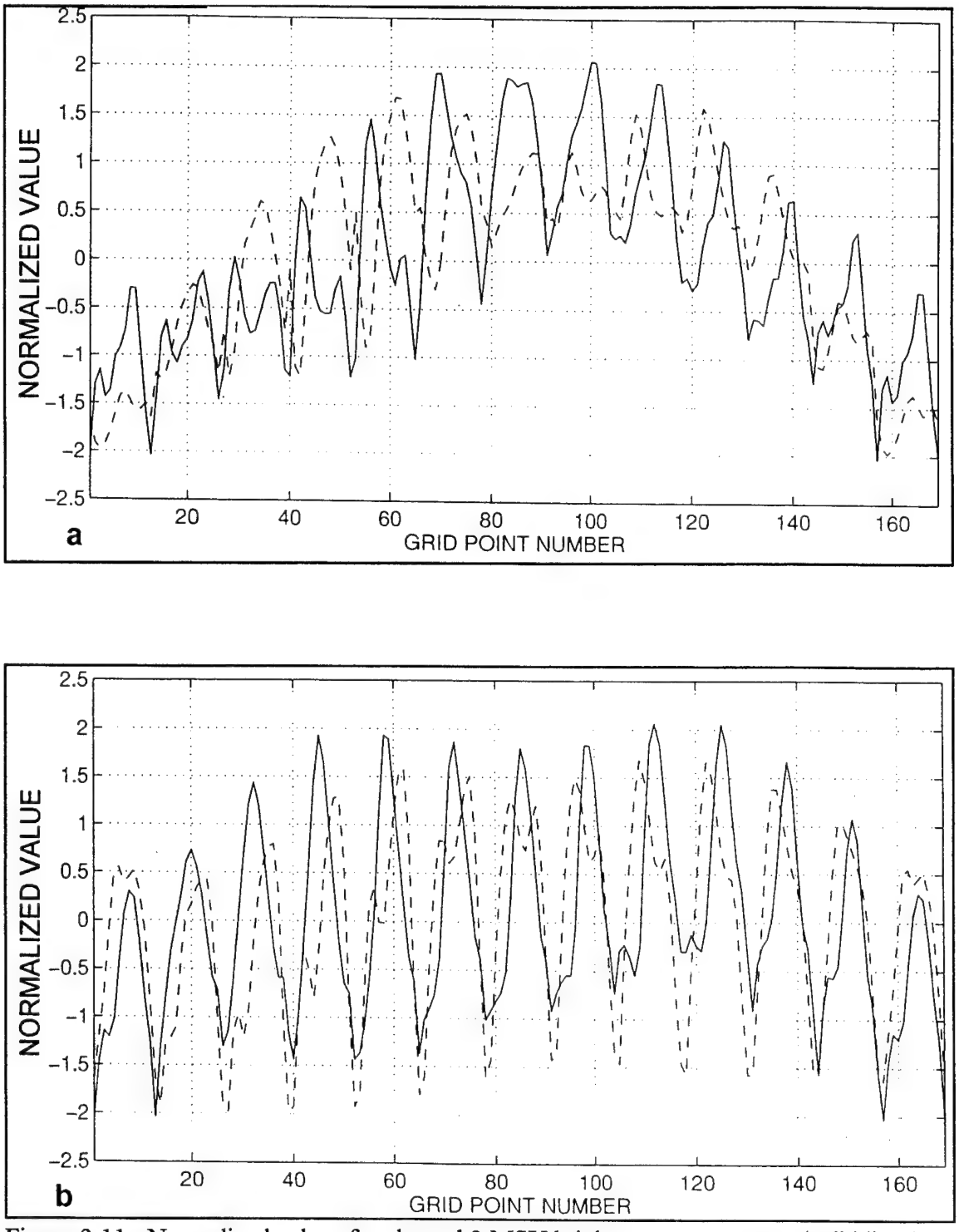

Figure 3.11. Normalized values for channel 3 MSU brightness temperature (solid lines) and 500-mb height (dashed lines) at each individual grid point in sub-domain 7 for the detrended 1200 UTC 10 March 1994 fields. Latitude method is depicted in (a), longitude method in (b).

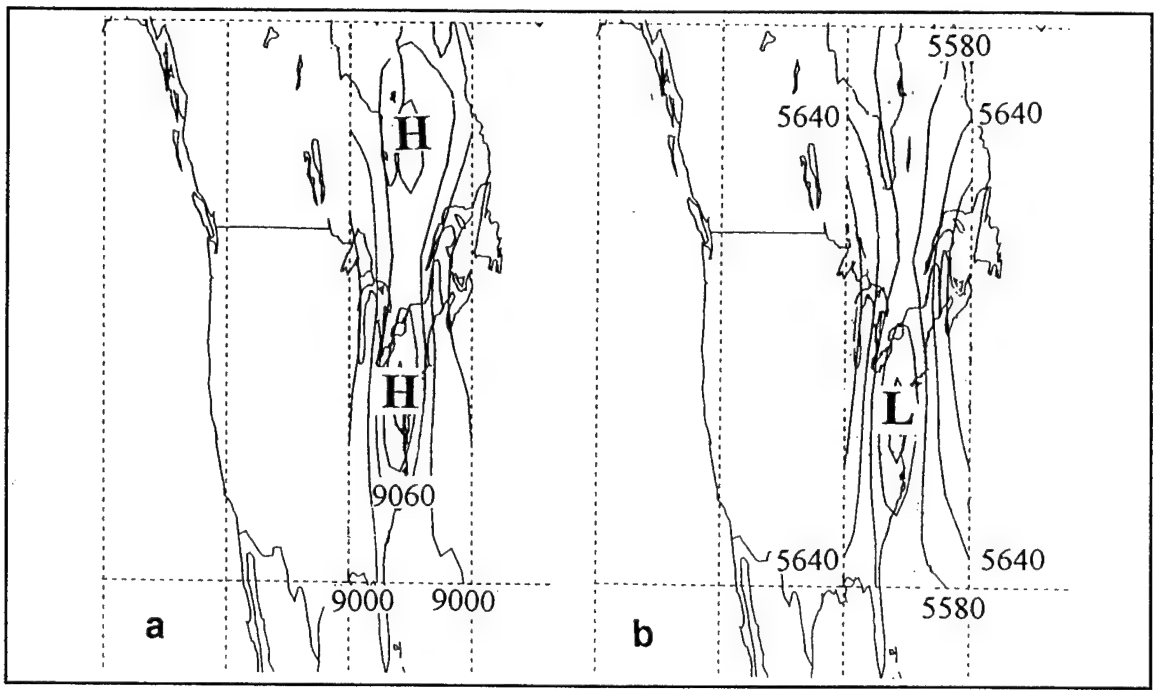

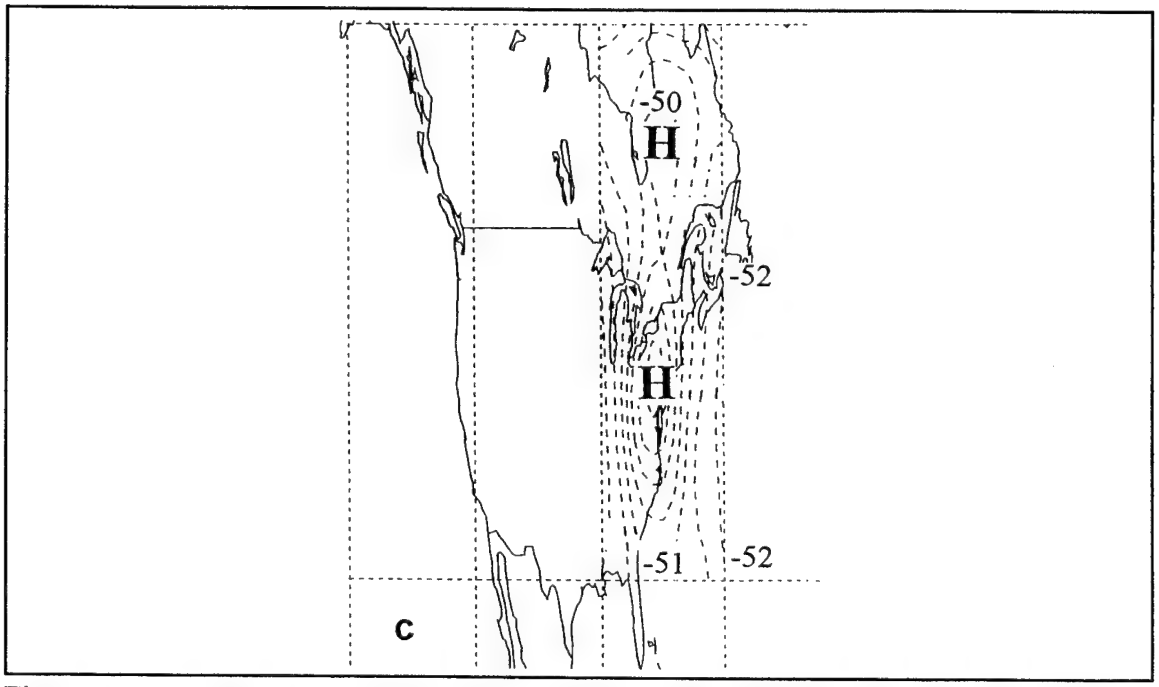

Figure 3.12. 1200 UTC 11 March 1994 analysis of detrended (a) 400-100-mb thickness (contour interval is 60 m), (b) 500-mb height (contour interval is 60 m), and (c) channel 3 MSU brightness temperature (contour interval is 1° C) for sub-domain 7.

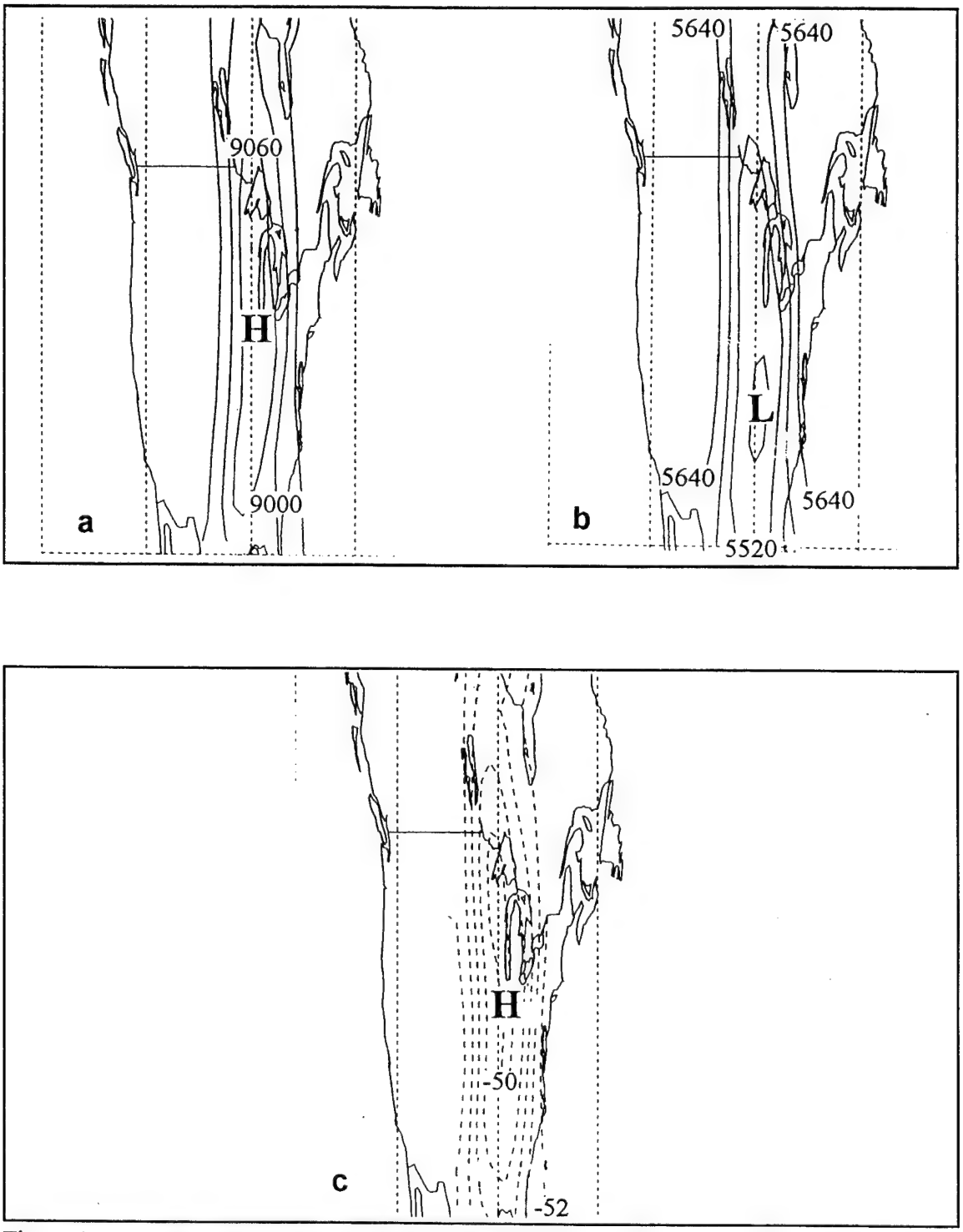

Figure 3.13. 1200 UTC 10 March 1994 analysis of detrended (a) 400-100-mb thickness (contour interval is 60 m), (b) 500-mb height (contour interval is 60 m), and (c) channel 3 MSU brightness temperature (contour interval is 1° C) for modified sub-domain 7, shifted 15° west of the original sub-domain.

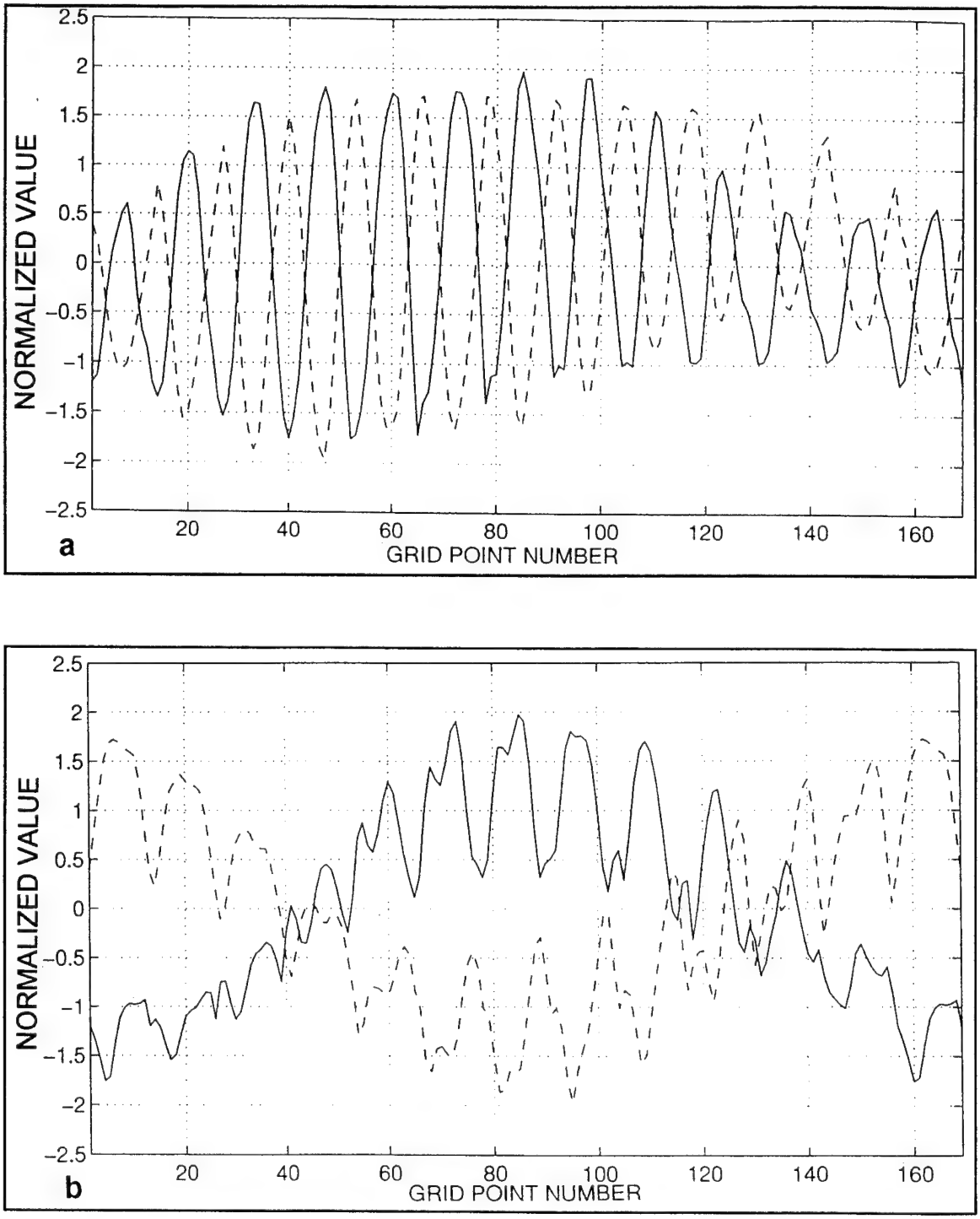

Figure 3.14. Normalized values for channel 3 MSU brightness temperature (solid lines) and 500-mb height (dashed lines) at each individual grid point in the modified sub-domain 7 for the detrended 1200 UTC 10 March 1994 fields. For these computations, the original sub-domain 7 was shifted 15° westward. Latitude method is depicted in (a), longitude method in (b).

IV. CASE STUDIES

In this chapter, two case studies will be presented. These case studies demonstrate the usefulness of MSU data in providing the operational weather forecaster with a reliable description of the current state of the atmosphere and as a tool to judge the accuracy of numerical weather prediction models.

A. MAY 1995

A 24-h period from 0000 UTC 12 to 0000 UTC 13 May 1995 illustrates the usefulness of MSU analyses in the interpretation of Numerical Weather Prediction (NWP) forecasts. During this time period, the Navy Operational Global Atmospheric Prediction System (NOGAPS), the National Weather Service (NWS) Nested Grid Model (NGM) and the NWS Eta models predicted a significant rain event for central California to begin sometime after 1200 UTC on 13 May. This precipitation was predicted to be associated with a large disturbance advancing southeastward from the Gulf of Alaska. Although the precipitation, including thunderstorm activity, did actually occur, it did so 19 h earlier (1700 UTC on 12 May) than expected. Moreover, this precipitation was associated with a short wave trough ahead of the main disturbance that was not predicted by any of the NWP products. This case study will examine the model forecasts and the MSU analyses to determine if the latter could have indicated the shortwave and the earlier onset of precipitation.

Since the three NWP forecasts were very similar, only the Eta products are shown here. Figure 4.1 presents the 500-mb 24-h forecast valid at 0000 UTC 13 May. An elongated area of positive vorticity extends from the Gulf of Alaska through northern California and into western Nevada. However, very little positive vorticity advection (PVA) is evident over California. Twelve hours later, the 12-h forecast, also valid at 0000 UTC 13 May (Fig. 4.2) shows the same general pattern of positive vorticity and heights and still no significant PVA over California.

As opposed to the 24-h forecasts, the verifying analysis (Fig. 4.3) shows a well developed vorticity maximum over northern California and PVA over central California. This analysis is the first indication of a separate short wave in the NWP products and emphasizes the difficulty of west coast forecasting. The chart implies that precipitation had been falling over central California for several hours before this 0000 UTC time, which is verified by the 1735 UTC 12 May national radar summary (Fig. 4.4). Note the area of rainshowers and thunderstorms over central California. As evidenced by the surface progs (Fig. 4.5 and 4.6), forecasters were following the NWP products closely. Specifically, no precipitation was predicted over the San Francisco Bay area through 0000 UTC 13 May.

The satellite imagery during the time period illustrates the formation and movement of the short wave that caused the early precipitation. Figure 4.7 is an infrared (IR) image from 1130 UTC 12 May. An area of cloudiness is evident just offshore of northern California and Oregon. By 1630 UTC, a comma shape is clearly present in the clouds (Fig. 4.8) centered near 42 N 128 W. The 2000 UTC satellite image (Fig. 4.9) shows the comma even more clearly, with the cloud band extending well inland over California. Satellite data from

2300 UTC (not shown) indicate the comma is almost completely onshore. Although the comma cloud suggests the presence of a short wave crossing the coast earlier than the NWP forecasts, confirmation of this wave development would be very welcome by the forecaster.

Figure 4.10 shows a series of full resolution (110 km) MSU analyses from 0200 UTC 12 to 0200 UTC 13 May, derived from NOAA polar-orbiting satellite passes. In Fig. 4.10a a pronounced warm anomaly associated with the unstable wave is present just offshore Victoria Island, with a center temperature greater than -45° C. An extension of warmer air reaches southeastward over California. This pattern is consistent with other documented cases of the extrusion of relatively warm stratospheric air into the mid troposphere prior to rapid surface development (Uccellini et. al, 1985; Boyle and Bosart, 1986; Reed and Albright, 1986; Whittaker et. al, 1988). By 1600 UTC 12 May (Fig. 4.10b) the center of the anomaly has moved southeastward, maintaining its core temperature. The temperature in the southeastward extending trough has increased since 0200 UTC, indicating warm advection or subsidence over the western states. At 0200 UTC 13 May (Fig. 4.10c) the center is near the coast of Oregon and appears to be nearly vertically stacked with the surface low. The MSU data at 0200 UTC is in strong agreement with visual and IR imagery indicating the presence of the new short wave trough.

There is another key feature of the MSU analyses that becomes clear when comparing them to the corresponding 200-mb analysis at 0000 UTC and 1200 UTC 12 May (Figs. 4.11 and 4.12). Notice the pattern of heights and isotherms off the Pacific west coast. They are completely in phase, indicating little or no warm air advection in the upper levels of the troposphere. However, the orientation of the MSU isotherms is much more west-east

oriented. Hence, when the height pattern is overlayed on the MSU analysis a large amount of warm air advection is found in the same area. Hirschberg and Fritsch (1991a, b) document this warm advection as leading to maximum surface development under favorable lower tropospheric conditions.

In conclusion, it is shown that by using the MSU information, specifically the 0200 UTC 12 May analysis, and IR satellite imagery, the timing error of the NWP products can be seen at least 12 hours prior to the onset of precipitation over central California.

B. JANUARY 1995

A weather event similar to the May 1995 case described above occurred during the period 1200 UTC 25 to 0000 UTC 27 January 1995. In this case however, NOGAPS performed significantly better than the NGM. As we will see, MSU information supports the NOGAPS solution. Hence, the MSU analysis potentially gives forecasters another tool to help them chose between widely differing model solutions.

The 48-h 500-mb NGM forecast valid 0000 UTC 27 January (Fig. 4.13) shows a weak trough over Washington state, but negative vorticity advection (NVA) over northern California. The 36-h 500-mb NGM forecast valid at the same time (Fig. 4.14) shows a similar height pattern. Although the 36-h NGM exhibits a greater amount of positive vorticity associated with the short wave it, like the 48-h NGM distinctly shows NVA over northern and central California. The 24-h 500-mb NGM forecast (Fig. 4.15) continues to increase the amount of positive vorticity associated with the short wave and also shows a slight amount

of positive vorticity advection (PVA) over northern California. The 12-h 500-mb NGM forecast (Fig. 4.16) is similar to the 24-h forecast, still not suggesting significant development for central California. The verifying analysis (Fig. 4.17) shows a closed 5430 m low just offshore of northern Oregon and a sharp positive vorticity trough indicating strong PVA over central California.

The same series of forecast charts from NOGAPS provides a better set of forecasts. The 48-h forecast valid 0000 UTC 27 January (Fig. 4.18a) has a 500-mb trough similar to the NGM (Fig.4.12). Although it is not as deep as the one indicated on the NGM, it displays a significant amount of PVA through northern and central California. In addition, areas of >90% RH at 700 mb are clearly shown over California (Fig. 4.18b). The subsequent model runs continue to forecast and deepen this wave. Clearly, the NOGAPS guidance handles this feature correctly out to 48 hours.

A series of satellite images shows the development and progression of this significant short wave. The 0234 UTC 26 January channel 4 IR picture (Fig. 4.19) has a cyclonically curved area of enhanced convection in the vicinity of 132° W. This is the developing comma cloud that will bring precipitation to central California. By 1634 UTC a well developed comma cloud with a center of circulation near the California - Oregon border is clearly shown (Fig. 4.20).

The MSU analyses corresponding to the satellite imagery begin with the 0200 UTC 26 January analysis (Fig. 4.21a). The characteristic warm pool associated with the developing short wave is present offshore of Oregon. As in the May case (Fig. 4.10), a warm trough extends well into southern California. This would suggest the movement of disturbed weather

into at least central California, confirming the NOGAPS solution and making the NGM solution questionable. The warm trough continues to move eastward and by 1600 UTC 26 January the anomaly is nearly vertically stacked with the surface low (Fig 4.21b). This figure also shows that this feature is separate from the larger storm which is still well back over the Pacific.

The 200-mb analysis for 0000 UTC 26 January (Fig. 4.22), in contrast to the May case, shows significant warm air advection in the upper troposphere. The January conventional analysis, as supported by the MSU information, more accurately depicts what is happening in the upper troposphere along the west coast than the May analysis (Figs. 4.11 and 4.12).

In these two case studies, the usefulness of real-time MSU data has been demonstrated. Used in conjunction with conventional data and satellite imagery, the MSU can be used to validate the performance of NWP solutions over data sparse regions.

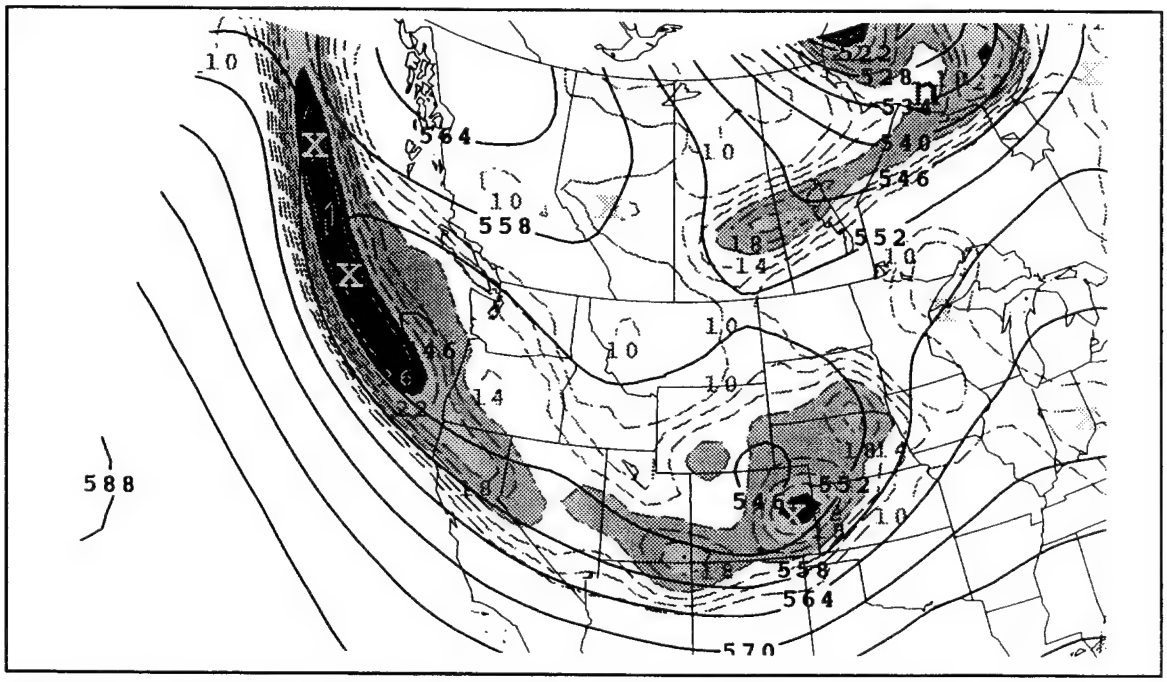

Figure 4.1. NWS Eta model 24-h forecast of 500-mb height (s, contour interval is 60 m) and absolute vorticity (d, contour interval is 2 x 10^{-5} s^{-1}) verifying at 0000 UTC 13 May 1995.

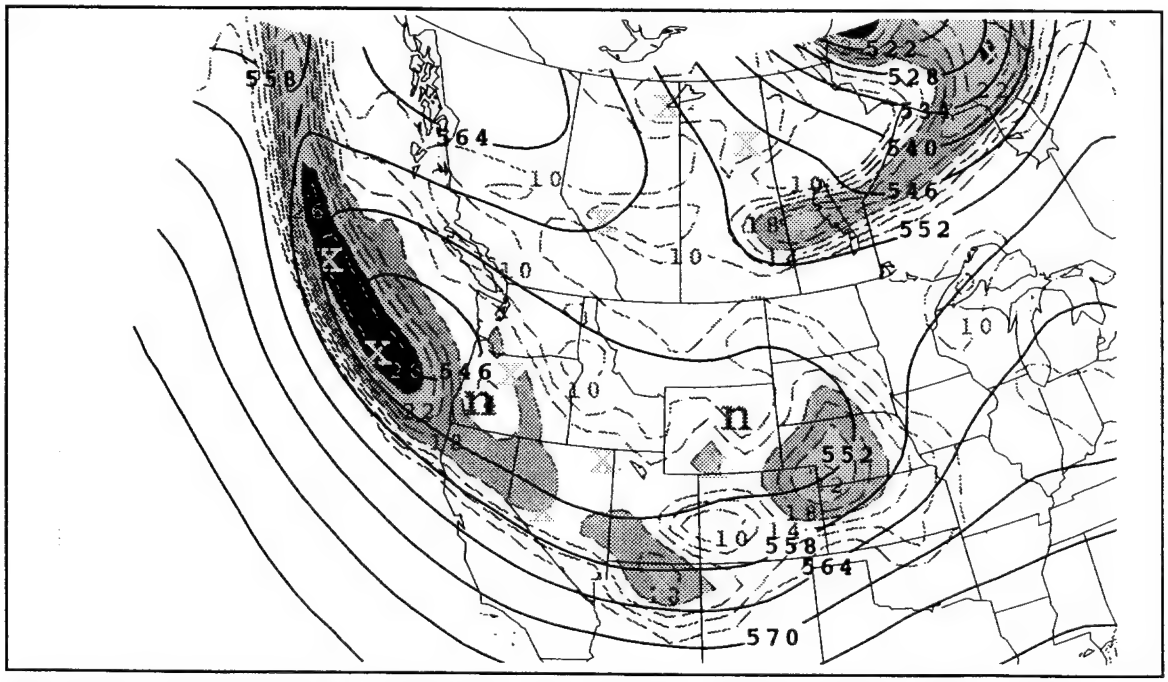

Figure 4.2. Same as Fig 4.1 except for 12-h forecast verifying at 0000 UTC 13 May 1995.

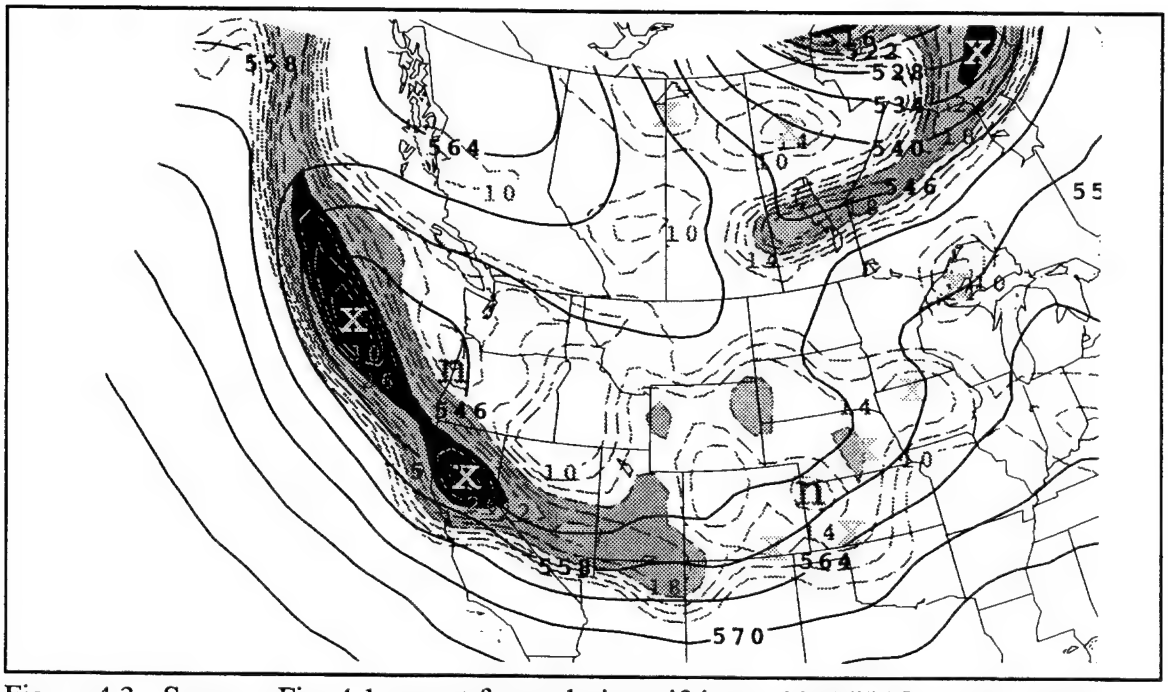

Figure 4.3. Same as Fig. 4.1 except for analysis verifying at 0000 UTC 13 May 1995.

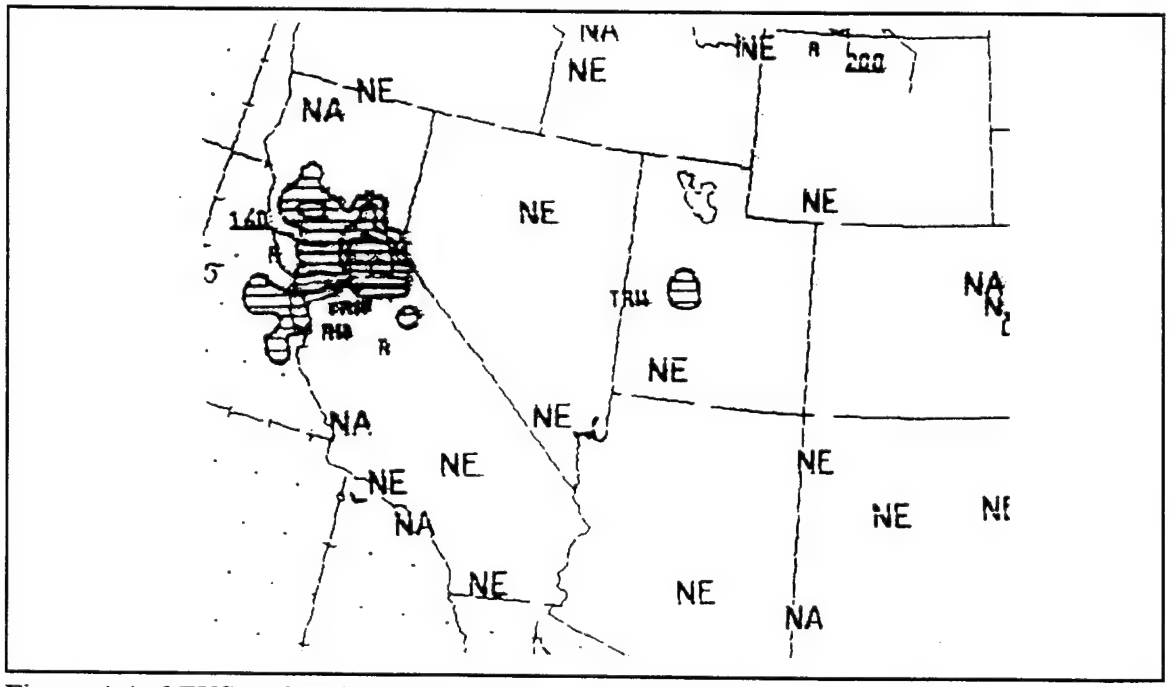

Figure 4.4. NWS national radar summary valid 1735 UTC 12 May 1995.

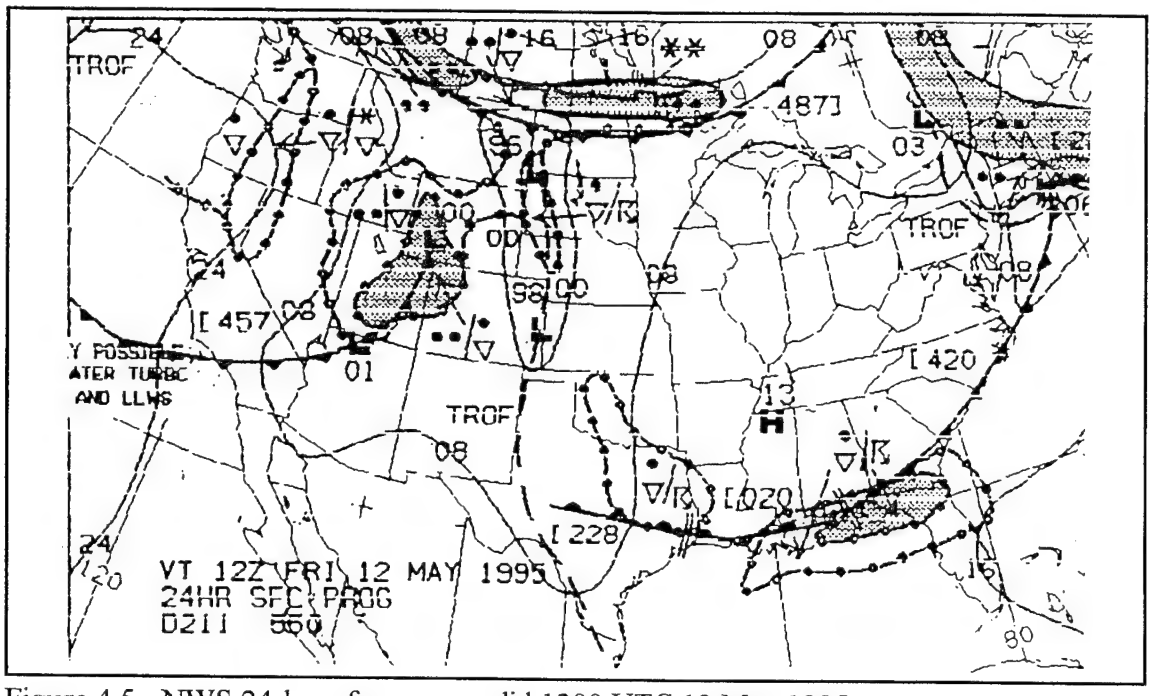

Figure 4.5. NWS 24-h surface prog valid 1200 UTC 12 May 1995.

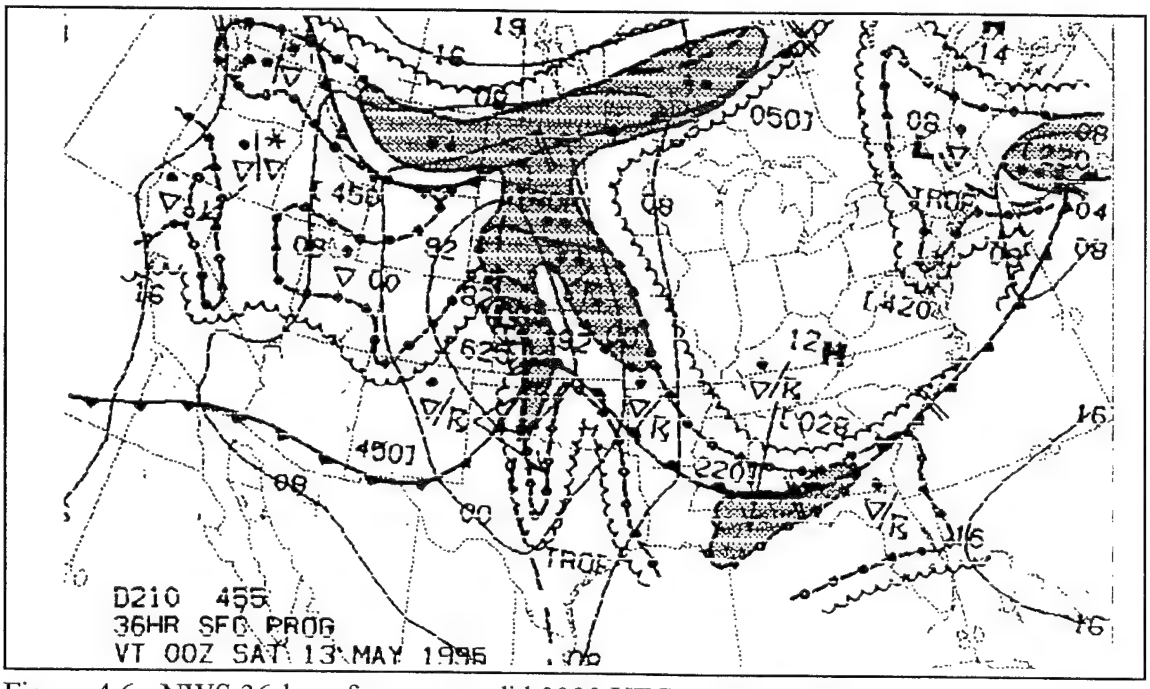

Figure 4.6. NWS 36-h surface prog valid 0000 UTC 13 May 1995.

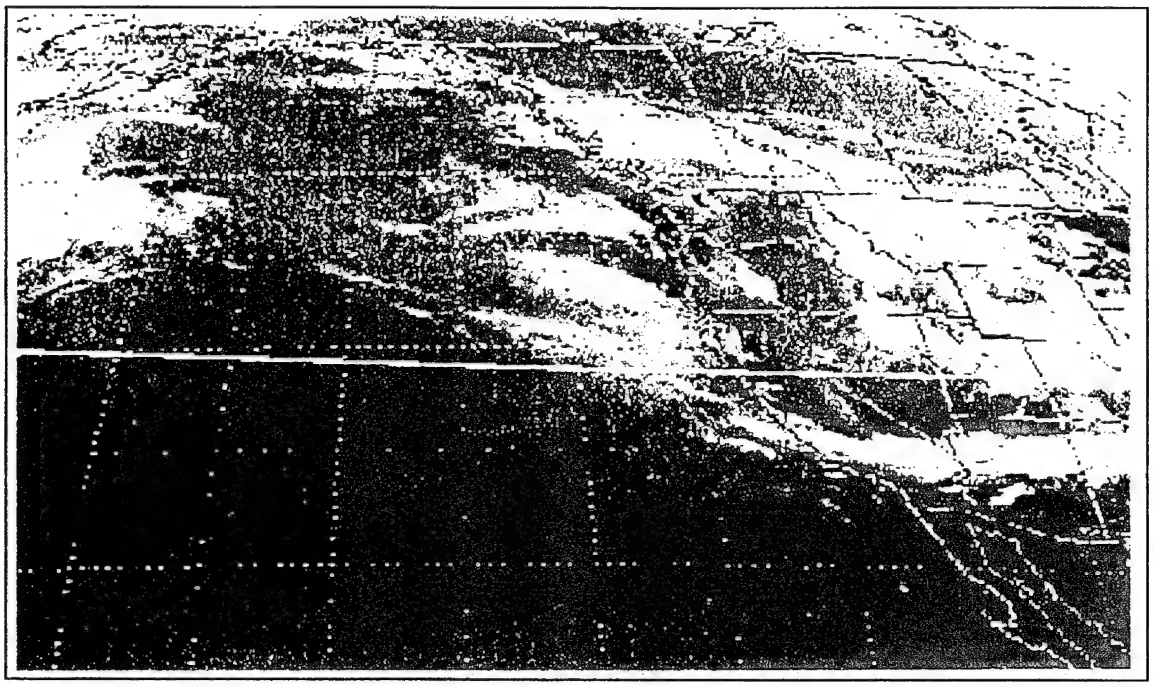

Figure 4.7. 1130 UTC 12 May 1995 infrared satellite image.

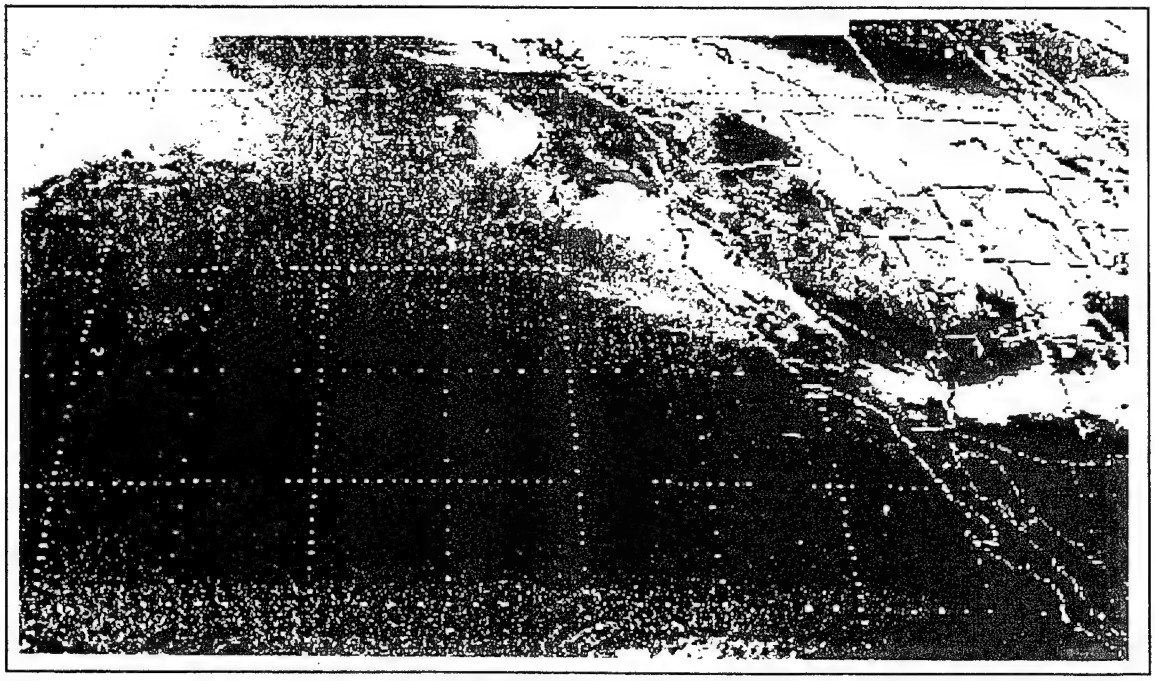

Figure 4.8. 1630 UTC 12 May 1995 infrared satellite image.

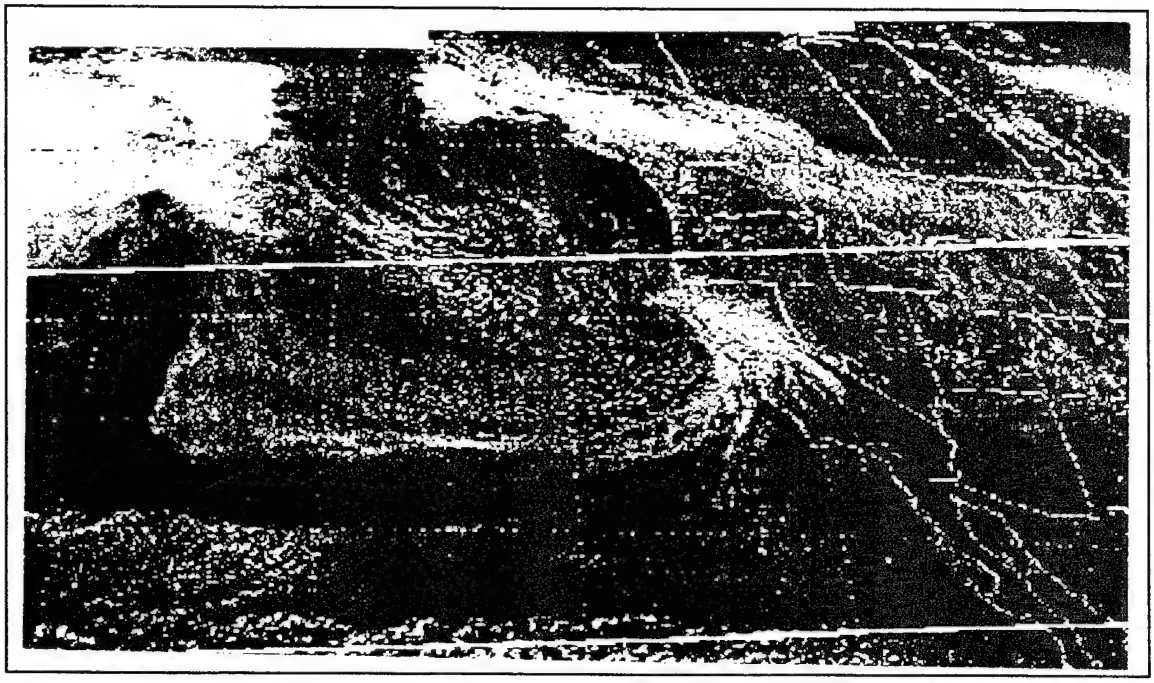

Figure 4.9. 2300 UTC 12 May 1995 visible satellite image.

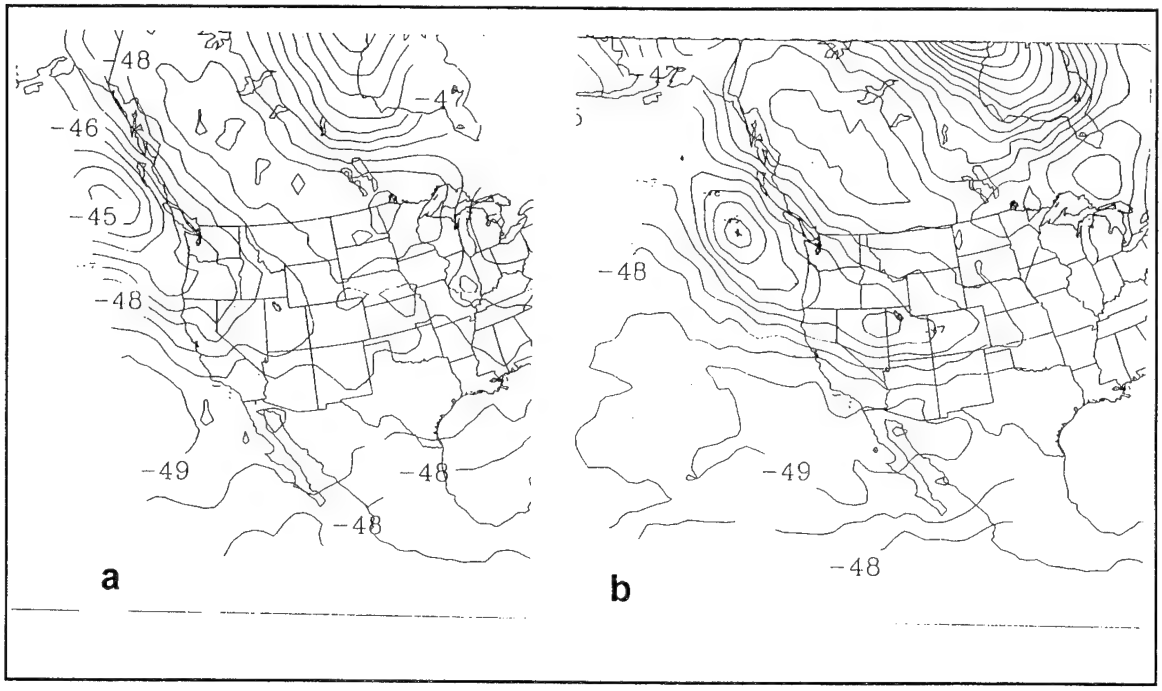

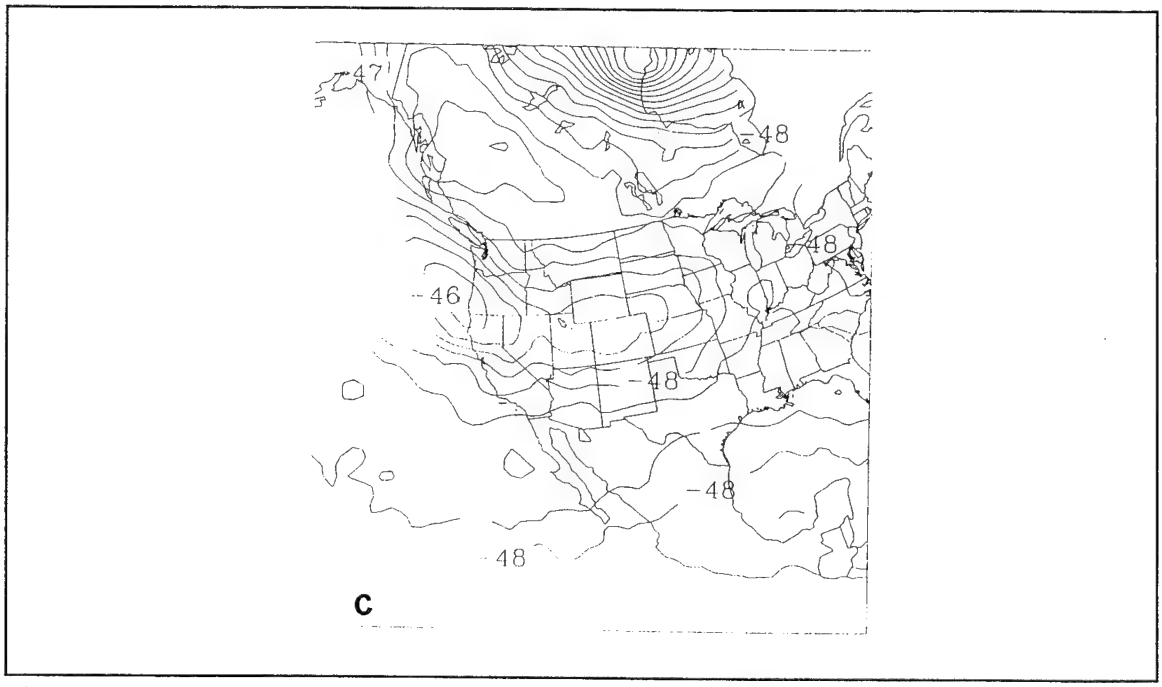

Figure 4.10. Full resolution (110 km) channel 3 MSU brightness temperature (contour interval is 0.5° C) analyses from NOAA-12 and NOAA-14 valid at (a) 0200 UTC 12 May 1995, (b) 1600 UTC 12 May 1995, and (c) 0200 UTC 13 May 1995.

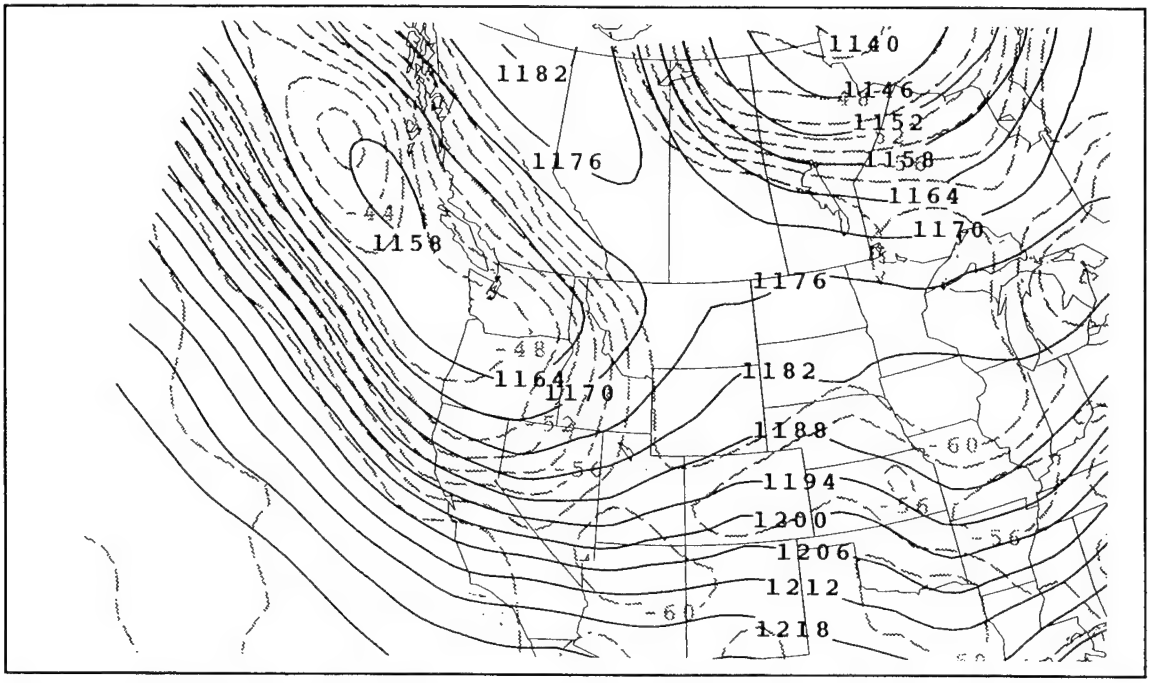

Figure 4.11. NWS Eta model 200-mb analysis for 000 UTC 12 May 1995 of height (s, contour interval is 120 m) and temperature (d, contour interval is 2° C).

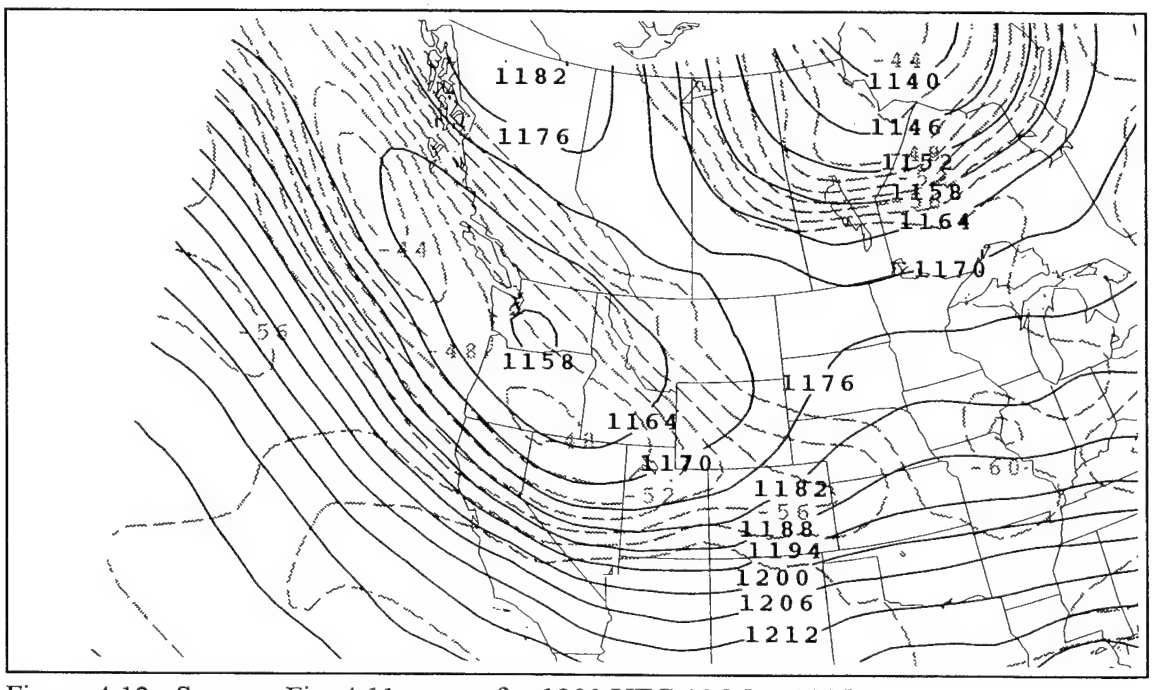

Figure 4.12. Same as Fig. 4.11 except for 1200 UTC 12 May 1995.

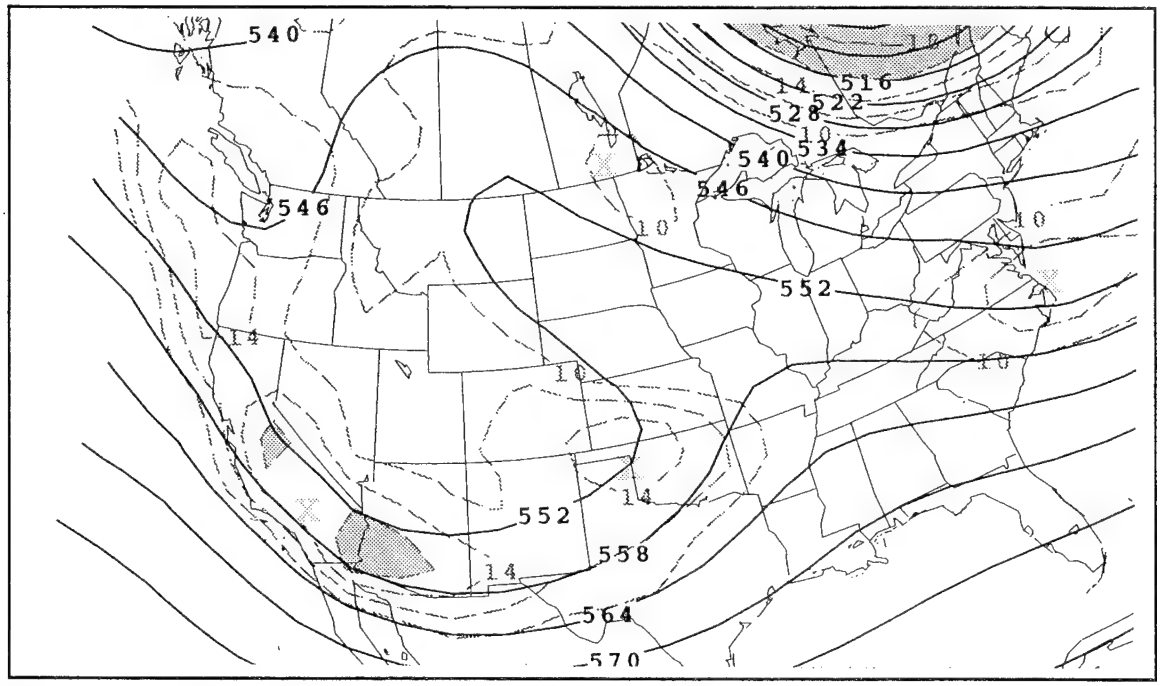

Figure 4.13. NWS NGM 48-h forecast of 500-mb height (s, contour interval is 60 m) and absolute vorticity (d, contour interval is 2 x 10^{-5} s^{-1}) verifying at 0000 UTC 27 January 1995.

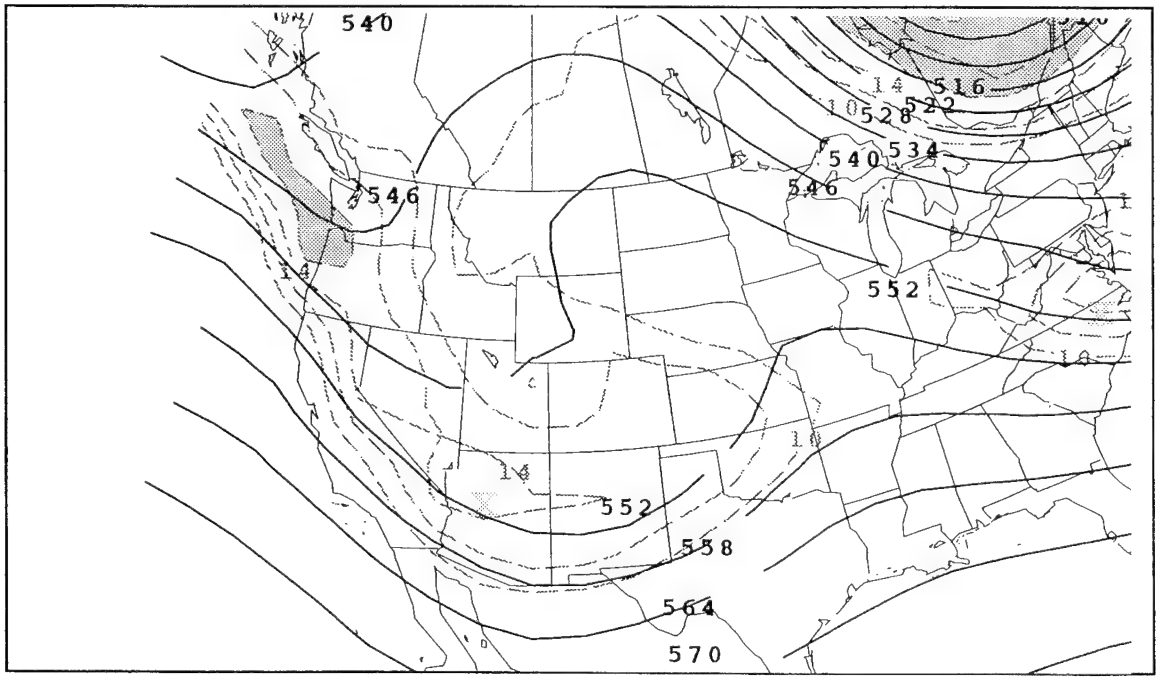

Figure 4.14. Same as Fig. 4.13 except for 36-h forecast verifying at 0000 UTC 27 January 1995.

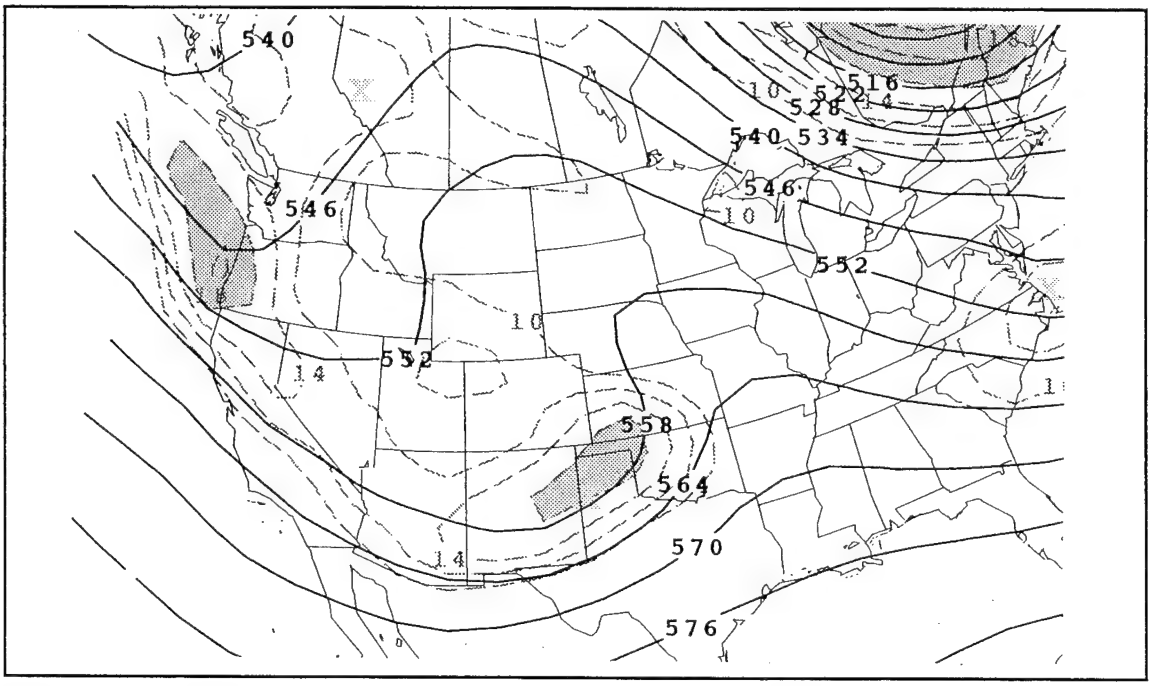

Figure 4.15. Same as Fig. 4.13 except for 24-h forecast verifying at 0000 UTC 27 January 1995.

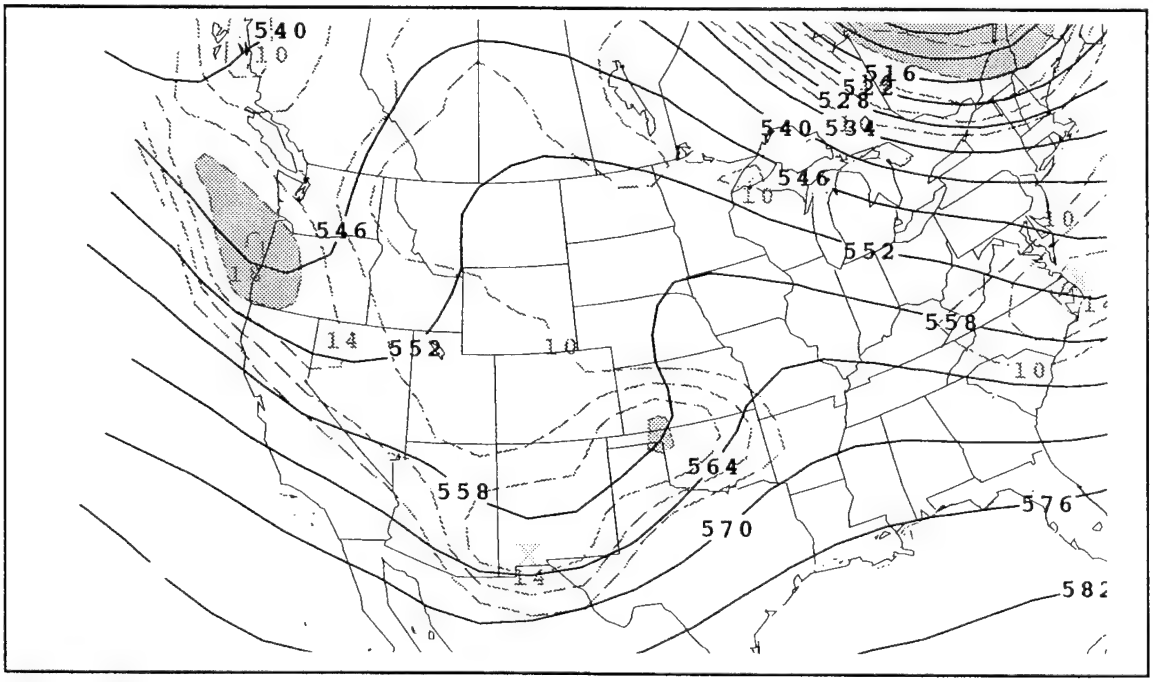

Figure 4.16. Same as Fig. 4.13 except for 12-h forecast verifying at 0000 UTC 27 January 1995.

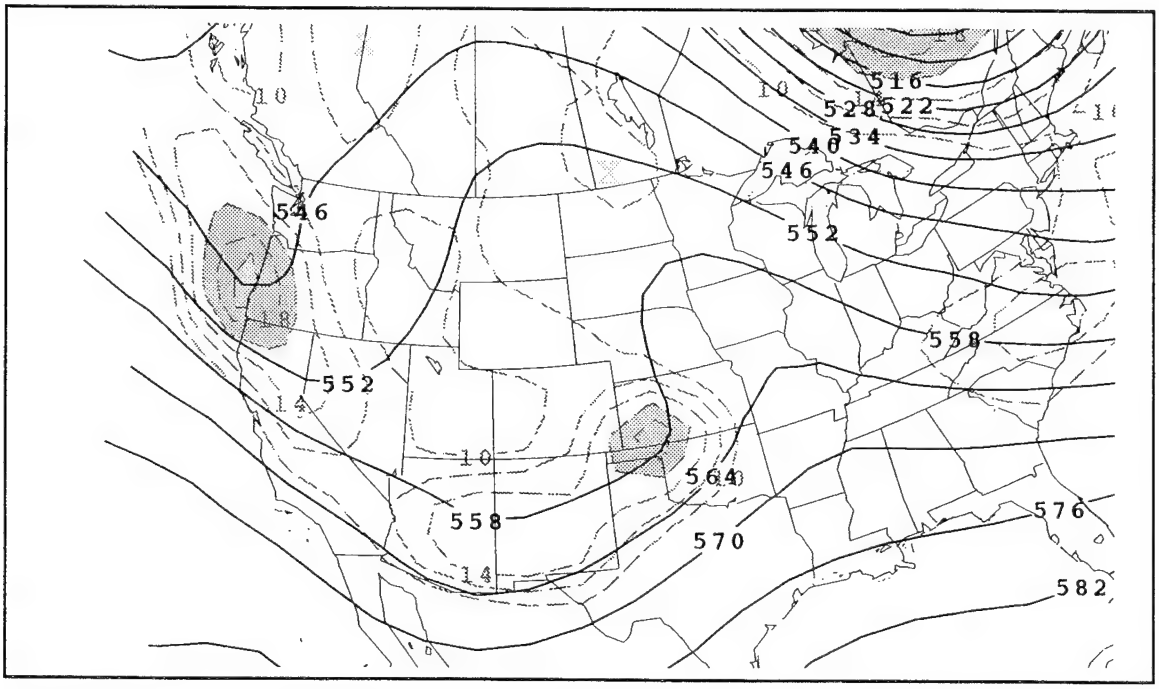

Figure 4.17. Same as Fig. 4.13 except for analysis verifying at 0000 UTC 27 January 1995.

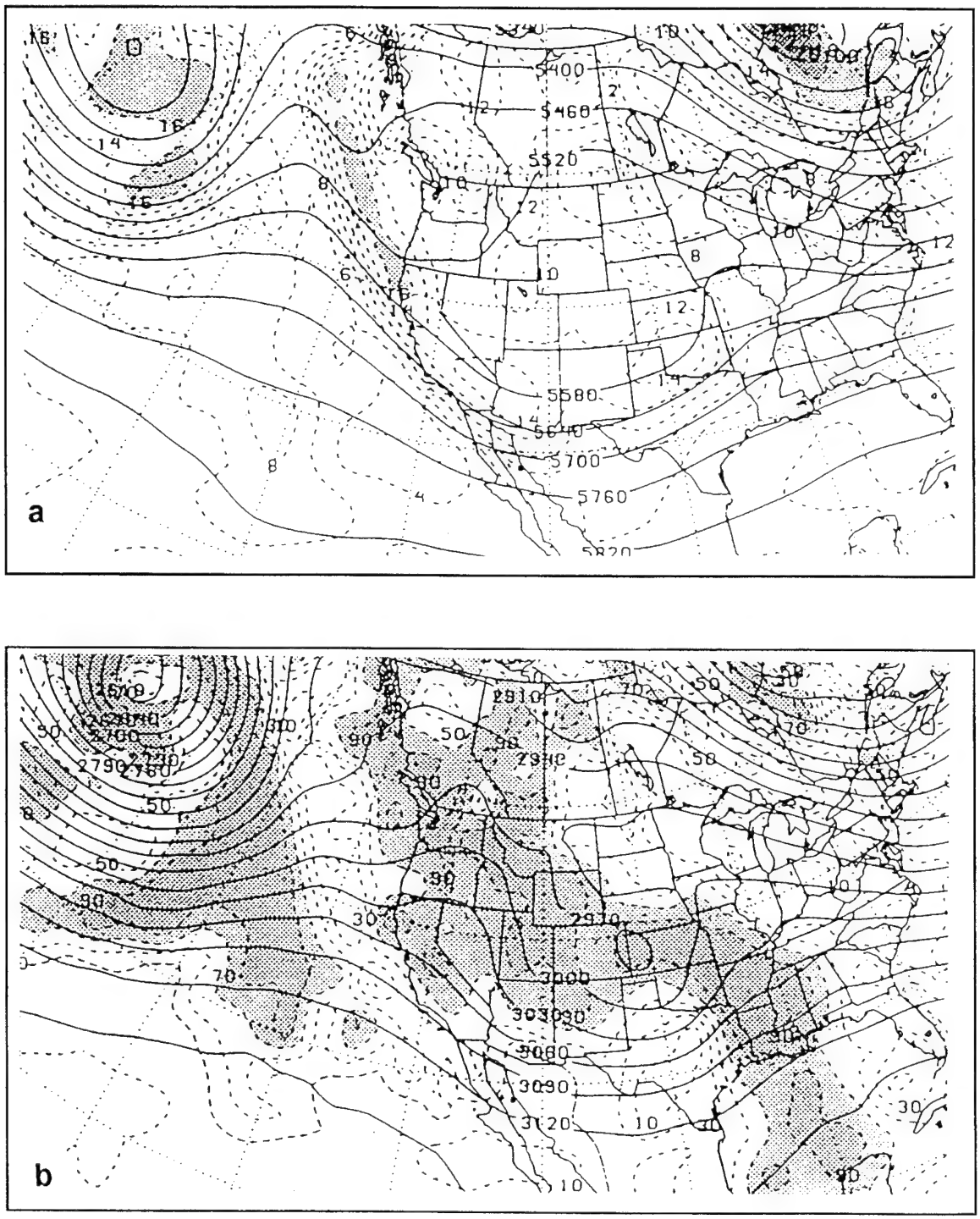

Figure 4.18. NOGAPS 48-h forecast of (a) 500-mb height (s, contour interval is 60 m) and absolute vorticity (d, contour interval is 2 x 10^{-5} s^{-1}) and (b) 700-mb height (s, contour interval is 60 m) and relative humidity (d, contour interval is 20%) verifying at 0000 UTC 27 January 1995.

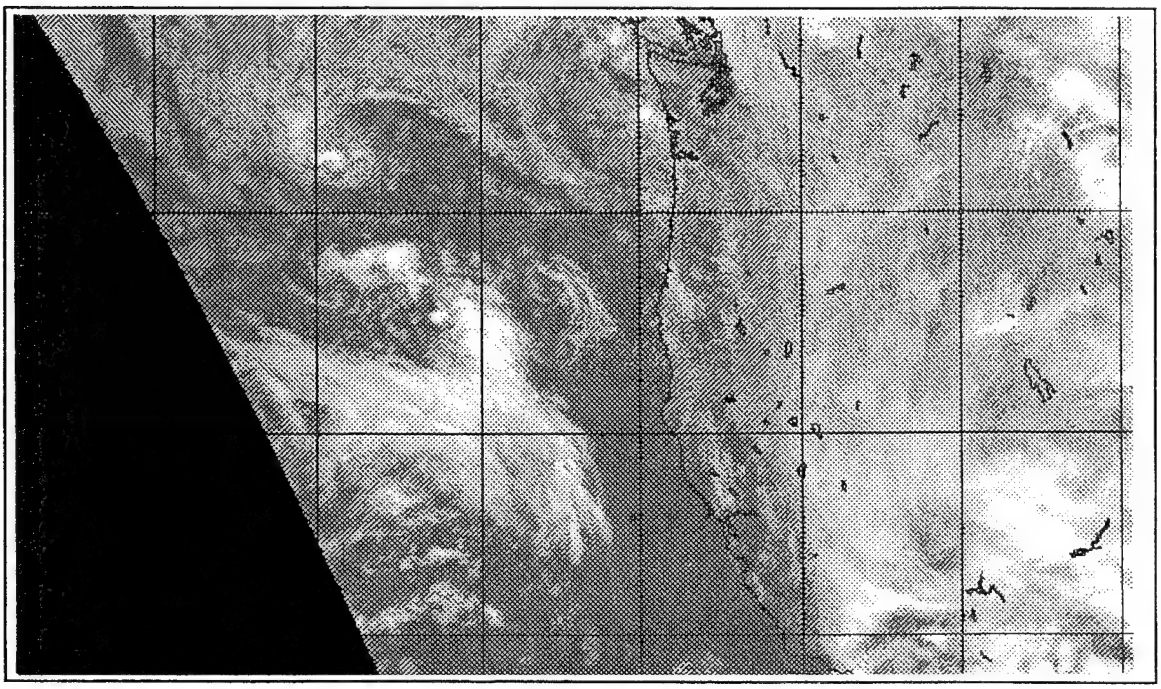

Figure 4.19. 0234 UTC 26 January 1995 infrared satellite image.

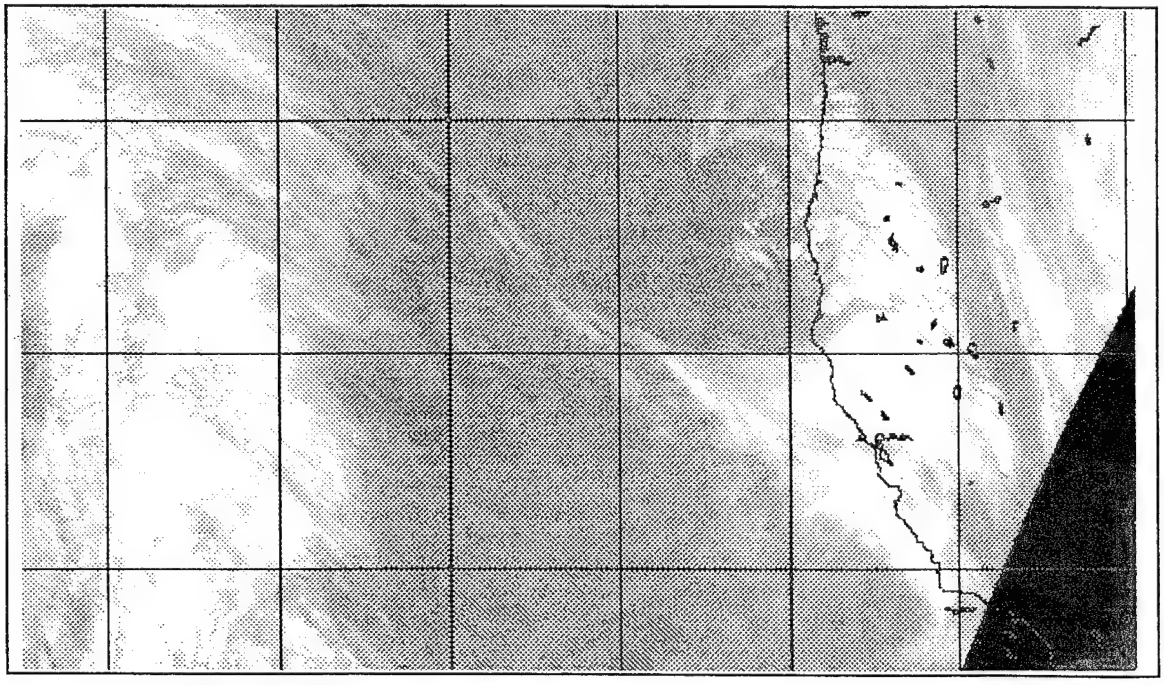

Figure 4.20. 1634 UTC January 1995 infrared satellite image.

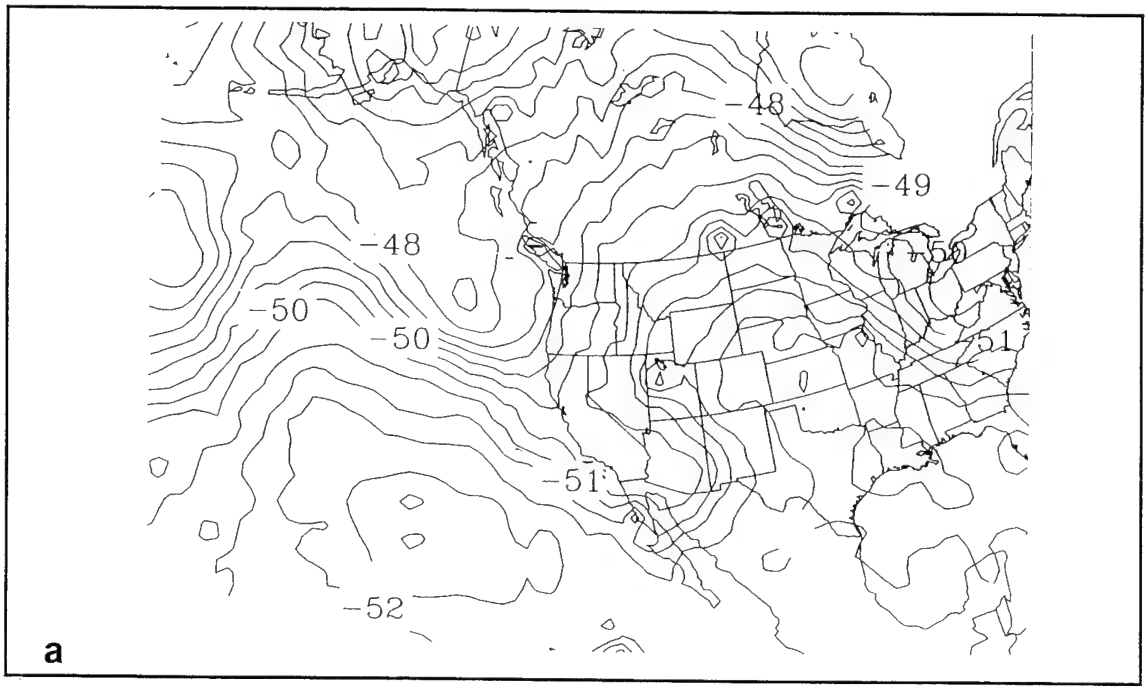

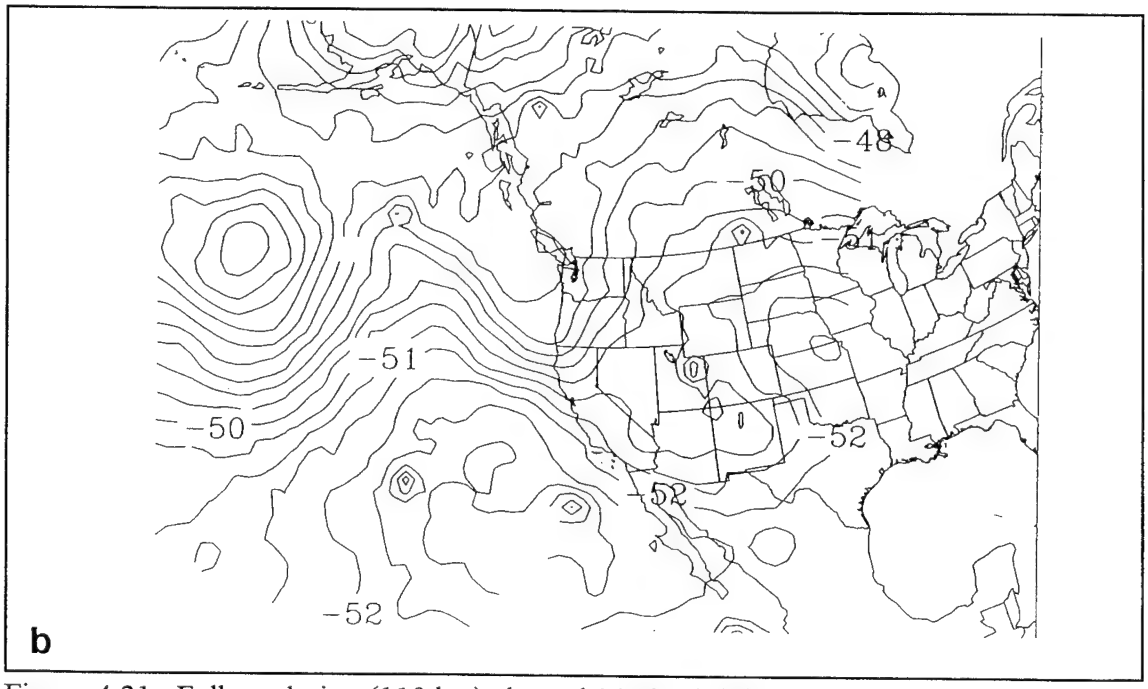

Figure 4.21. Full resolution (110 km) channel 3 MSU brightness temperature analyses from NOAA-12 and NOAA-14 valid at (a) 0200 UTC 26 January 1995 and (b) 1600 UTC 26 January 1995.

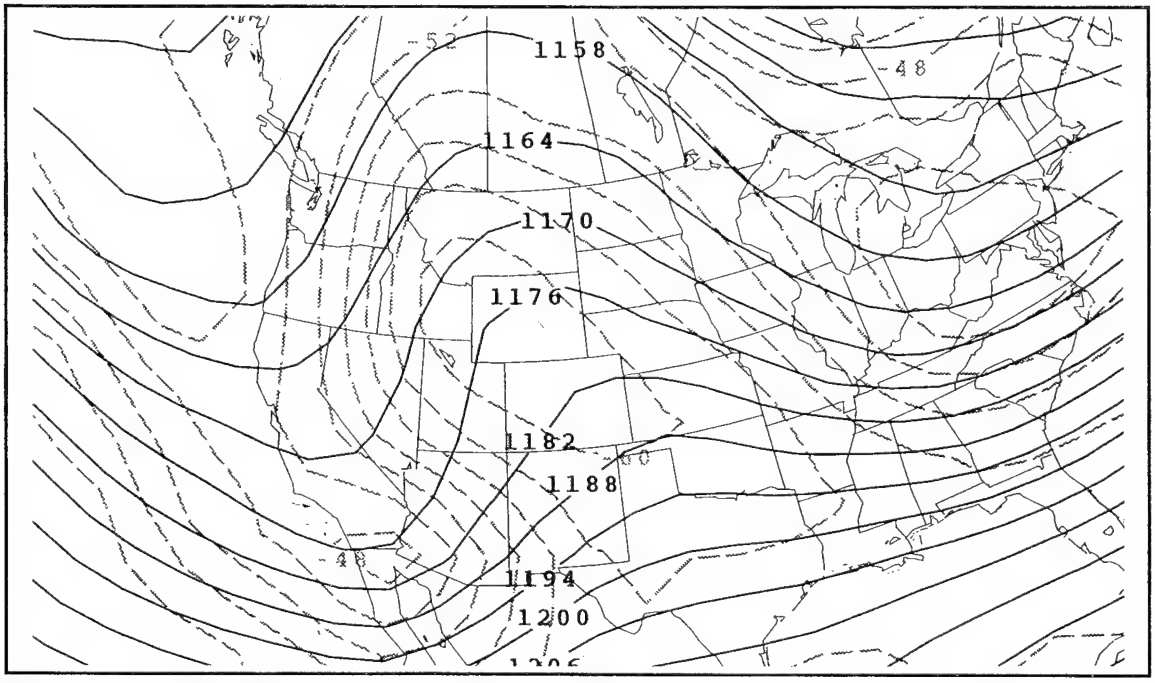

Figure 4.22. NOGAPS 200-mb analysis for 0000 UTC 26 January 1995 of height (s, contour interval is 120 m) and temperature (d, contour interval is 2° C).

V. CONCLUSIONS AND RECOMMENDATIONS

Parke (1994) found statistically-significant spatial and temporal correlations between channel 3 MSU brightness temperature and various conventional fields for a six-month period over the Northern Hemisphere. He concluded that these correlations provided quantitative evidence of the usefulness of the MSU as a tool in nowcasting and forecasting baroclinic waves. However, there were times during the six-month period when the correlation values were not as expected from theory. In this thesis, some of these infrequent unexpected correlations were examined to better understand possible limitations of the MSU tool. In particular, three potential problems were focused on in regard to the MSU-500-mb height and MSU-50-mb height correlations obtained by Parke (1994). These problems were: data limitations, synoptic pattern sensitivity and statistical methods.

Erroneous data certainly was one source of error. In one instance, an unexplained positive correlation between the small-scale "detrend" MSU and 500-mb height field was caused by an error in the MSU analysis field that was not caught by the objective error check routine. The MSU field had a bulls-eye pattern in the isopleths in the southwest corner of the sub-domain caused by an erroneous data point. This led to further problems when the scale-separation method attempted to make the data periodic around this erroneous value.

It was found that a thermal wind zonal index had some merit in identifying synoptic regimes that lead to reliable MSU correlations. Specifically, sub-domains having a negative zonal index showed a relatively high (>.65) correlation between the zonal index and the large-

scale "trend" MSU-50-mb height and the detrend MSU-500-mb correlations.

There were also problems with the statistical method used by Parke. The Eulerian method of defining sub-domains was reliable in most but not all cases. When a prominent meteorological feature such as a deep trough or pronounced ridge was located at the boundary of a sub-domain, the correlations proved questionable. Simply moving the sub-domain such that the feature was more in the center of the domain vastly improved the correlation. In one instance, a detrend MSU-500-mb correlation changed from a 0.60 to a -0.98 simply by shifting the sub-domain in this way.

The Errico (1985) linear detrending method was found to be not always successful in eliminating unwanted scale signals. Specifically signals with wavelengths equal to twice the sub-domain size were not eliminated by the method. On several occasions, this larger-scale signal dominated the correlation.

The determination of area correlation coefficients by averaging individual latitude or longitude correlations within a sub-domain produced more expected correlations than the total area average when certain east-west or north-south gradients were present. Over the entire six-month data set however, the total area average method worked best.

Finally, to show the utility of the MSU in nowcasting and forecasting situations, two case studies were performed. These showed that the MSU data was valuable when used in conjunction with satellite imagery and numerical weather prediction (NWP) products in forecasting developing baroclinic waves. In one instance, the MSU revealed a rapidly developing short wave that was very difficult to distinguish in IR imagery. In the second case, the MSU was useful in determining the correct solution from widely differing NWP solutions.

The findings of this thesis lead to several recommendations for further study:

1. Further research is needed to substantiate the preliminary evidence that the zonal index can be used as a stratifying tool to identify synoptic regimes in which the MSU is a less reliable tool for tracking mid-level waves. In addition, why certain regimes lead to stronger correlations than others needs more explanation.

2. A method to detrend the data by eliminating higher order signals is needed in cases where a linear detrend method such as Errico (1985) is inadequate.

3. A semi-Lagrangian method of statistically correlating the MSU and conventional field anomalies should be developed and implemented to evaluate the MSU tool.

4. The unexplained trend MSU-50-mb height correlation discrepancy between Eastern and Western Hemisphere results discussed by Parke (1994) appears to be synoptic regime and/or scale related. This thesis presented evidence that either or both could be a contributing factor. Further study into this question is needed to better determine the cause.

LIST OF REFERENCES

Boyle, J. S., and L. F. Bosart, 1986: Cyclone-anticyclone couplets over NorthAmerica. Part 2: Analysis of a major cyclone event over the eastern United States. *Mon. Wea. Rev.*, **114**, 2432-2465.

Carlson, T. N., 1994: *Mid-Latitude Weather Systems.* Rutledge, New York, 507 pp.

Errico, R. M., 1985: Spectra computed from a limited area grid. *Mon. Wea.Rev.*, **113**, 1554-1562.

Fujita, T. T., 1986: Mesoscale classifications: Their history and their application to forecasting. In *Mesoscale Meteorology and Forecasting*, P. S. Ray (Ed.), American Meteorological Society, Boston, 18-34.

Hirschberg, P. A., and J. M. Fritsch, 1991a: Tropopause undulations and the development of extratropical cyclones. Part I: Overview and observations from a cyclone event. *Mon. Wea. Rev.*, **119**, 496-517.

_____, and _____, 1991b: Tropopause undulations and the development of extratropical cyclones. Part II: Diagnostic analysis and conceptual model. *Mon. Wea. Rev.*, **119**, 518-550.

_____, and _____, 1993: On understanding height tendency. *Mon. Wea. Rev.*, **121**, 2646-2661.

Holton, J. R., 1979: *An introduction to Dynamic Meteorology*. Academic Press, NewYork, 391 pp.

Hoskins, B. J., M. E. McIntyre and A. W. Robertson, 1985: On the use and significance of isentropic potential vorticity maps. *Quart. J. Roy. Meteor. Soc.*, **111**, 877-946.

Janzow, P., 1992: *The Student Edition of Matlab*. Prentice Hall, Englewood Cliffs, New Jersey, 494 pp.

Machta, L., and E. Hughes, 1970: Atmospheric oxygen in 1967 to 1970. *Science*, **168**, 1582-1584.

Meeks, M. L., and A. E. Lilley, 1963: The microwave spectrum of oxygen in the earth's atmosphere. *J. Geophys. Res.*, **68**, 1683-1703.

Nuss, W. A., and D. W. Titley, 1994: Use of multiquadric interpolation for meteorological objective analysis. *Mon. Wea. Rev.*, **122**, 1611-1631.

Orlanski, I., 1975: A rational subdivision of scales for atmospheric processes. *Bull. Amer. Meteor. Soc.*, **56**, 527-530.

Parke, M. C., 1994: Comparison of satellite-derived MSU brightness temperatures and conventionally-derived fields. M. S. thesis, Naval Postgraduate School, Monterey, California, December, 1994.

Reed, R. J., and M. D. Albright, 1986: A case study of explosive cyclogenesis in the eastern Pacific. *Mon. Wea. Rev.*, **114**, 2297-2319.

Smith, W. L., H. M. Woolf, C. M. Hayden, D. Q. Wark, and L. M. McMillin, 1979: The TIROS-N operational vertical sounder. *Bull. Amer. Meteor. Soc.*, **60**, 1177-1187.

Spencer, R. W., J. R. Christy, and N. C. Grody, 1990: Global atmospheric temperature monitoring with satellite microwave measurements: Method and results, 1979-84. *J. Climate*, **3**, 1111-1128.

Spencer, R. W., W. M. Lapenta, F. R. Robertson, 1995: Vorticity and Vertical Motions Diagnosed from Satellite Deep-Layer Temperatures. *Mon. Wea. Rev.*, **123**, 1800-1810.

Uccellini, L. W., D. Keyser, K. F. Brill and C. H. Wash, 1985: The President's Day cyclone of 18-19 February 1979: Influence of upstream trough amplification and associated tropopause folding on rapid cyclogenesis. *Mon. Wea. Rev.*, **113**, 962-988.

Velden, C. S. 1992: Satellite-based microwave observations of tropopause-level thermal anomalies: Qualitative applications in extratropical cyclones events. *Wea. Forecasting*, 7, 669-682.

Whittaker, J. S., L. W. Uccellini and K. F. Brill, 1988: A model-based diagnostic study of the rapid development phase of the Presidents' Day cyclone. *Mon. Wea. Rev.*, **116**, 2337-2365.

INITIAL DISTRIBUTION LIST

1.	Defense Technical Information Center 8725 John J. Kingman Rd., STE 0944 Ft Belvoir, VA 22060-6218	2
2.	Library, Code 13 Naval Postgraduate School Monterey, CA 93943-5101	2
3.	Oceanography Department Code OC/CO Naval Postgraduate School 589 Dyer Rd Rm 252 Monterey, CA 93943-5122	1
4.	Meteorology Department Code MR/Hy Naval Postgraduate School 589 Dyer Rd Rm 252 Monterey, CA 93943-5122	1
5.	Dr. Paul A. Hirschberg Code MR/Hs Naval Postgraduate School 589 Dyer Rd Rm 252 Monterey, CA 93943-5122	4
6.	Dr. C. H. Wash Code MR/Wx Naval Postgraduate School 589 Dyer Rd Rm 252 Monterey, CA 93943-5122	3
7.	LT Mark W. Mickelinc Naval Postgraduate School 589 Dyer Rd Rm 216 Monterey, CA 93943-5122	1

8. Mr. Eric Thayler — 1
National Weather Service
10230 Smith Rd
Denver, CO 80239

9. Dr. Roy Spencer — 1
Earth System Science Division
NASA Marshall Space Flight Center
Huntsville, AL 35812

10. Dr.LeRoy Spayd — 1
National Weather Service
Services Evaluation Branch
W/OM21
1325 East-West Highway
Silver Spring, MD 20910

11. Dr. Louis Uccellini — 1
Director
Office of Meteorology
U. S. Department of Commerce
National Oceanic and Atmospheric Administration
National Weather Service
Silver Spring, MD 20910

12. Dr. Kim Richardson — 1
Naval Research Laboratory
7 Grace Hopper Ave Stop 2
Monterey, CA 93943-5502

13. Commander — 1
Naval Meteorology and Oceanography Command
1020 Balch Blvd
Stennis Space Center, MS 39529-5005

14. Commanding Officer — 1
Naval Oceanographic Office
Stennis Space Center, MS 39529-5001

15. Commanding Officer — 1
Fleet Numerical Meteorology and
Oceanography Center
7 Grace Hopper Ave Stop 4
Monterey, CA 93943

16. Commanding Officer — 1
Naval Oceanographic and Atmospheric
Research Laboratory
Stennis Space Center, MS 39529-5004

17. Superintendent — 1
Naval Research Laboratory
7 Grace Hopper Ave Stop 2
Monterey, CA 93943-5502